Heterojunction and Nanostructured Photovoltaic Device: Theory and Experiment

by

Kunal Ghosh

A Dissertation Presented in Partial Fulfillment
of the Requirements for the Degree
Doctor of Philosophy

Approved September 2011 by the
Graduate Supervisory Committee:

Stuart Bowden, Co-Chair
Christiana Honsberg, Co-Chair
Dragica Vasileska
Stephen Goodnick

ARIZONA STATE UNIVERSITY

December 2011

ABSTRACT

A primary motivation of research in photovoltaic technology is to obtain higher efficiency photovoltaic devices at reduced cost of production so that solar electricity can be cost competitive. The majority of photovoltaic technologies are based on p-n junction, with efficiency potential being much lower than the thermodynamic limits of individual technologies and thereby providing substantial scope for further improvements in efficiency. The thesis explores photovoltaic devices using new physical processes that rely on thin layers and are capable of attaining the thermodynamic limit of photovoltaic technology.

Silicon heterostructure is one of the candidate technologies in which thin films induce a minority carrier collecting junction in silicon and the devices can achieve efficiency close to the thermodynamic limits of silicon technology. The thesis proposes and experimentally establishes a new theory explaining the operation of silicon heterostructure solar cells. The theory will assist in identifying the optimum properties of thin film materials for silicon heterostructure and help in design and characterization of the devices, along with aiding in developing new devices based on this technology. The efficiency potential of silicon heterostructure is constrained by the thermodynamic limit (31%) of single junction solar cell and is considerably lower than the limit of photovoltaic conversion (~ 80 %). A further improvement in photovoltaic conversion efficiency is possible by implementing a multiple quasi-fermi level system (MQFL). A MQFL allows the absorption of sub band gap photons with current being extracted at a higher band-gap, thereby allowing to overcome the efficiency limit of single junction devices. A MQFL can be realized either by thin epitaxial layers of alternating higher and lower band gap material with nearly lattice matched (quantum well) or highly lattice mismatched (quantum dot) structure. The thesis identifies the material combination for quantum well structure and calculates the absorption coefficient of a MQFl based on quantum well. GaAsSb (barrier)/InAs(dot) was identified as a candidate material for MQFL using quantum dot. The thesis explains the growth mechanism of GaAsSb and the optimization of GaAsSb and GaAs heterointerface.

ACKNOWLEDGMENTS

First and foremost, I would like to thank my advisors Prof. Stuart Bowden and Prof. Christiana Honsberg for guiding and helping me through the course of my Ph.D. I would also like to express my gratitude to my committee members, Prof. Dragica Vasileska and Prof. Stephen Goodnick. Dr. Stephen Bremner, now at UNSW and Dr. Clarence Tracy helped in experimental work of my thesis and I would like to acknowledge their help. Finally, I would like to thank all my colleagues and friends at Solar Power laboratory and University of Delaware.

TABLE OF CONTENTS

LIST OF TABLES

LIST OF FIGURES

Figure Page

Figure Page

Chapter 1

INTRODUCTION

1.1 Background

Photovoltaic devices or solar cells convert sunlight into electrical energy. The photovoltaic effect was first discovered by A.E. Becquerel in 1839. In 1906, Albert Einstein formulated the interaction of light and matter through the photoelectric effect. The first photovoltaic cell was made by Bell laboratory based on diffused p-n junction technology. In this technology, doped silicon is used as the starting substrate (base of the solar cell) and p-n junction is created through the formation of an emitter region of complementary doping. The doping is performed by diffusion and the dopant is either in gas or liquid phase. The diffused silicon p-n junction technology has remained the dominant photovoltaic technology with incremental increase in efficiency over the years. The present day world record for efficiency of silicon solar cell is 24.7 %[1], which is based on diffused junction technology. The open circuit voltage (V_{oc}) even after elaborate optimization was limited to 720 mV in the devices. The V_{oc} in diffused junction solar cell actually has an upper limit of 720 mV due to the recombination current and is 100 mV lower than the thermodynamic limit[2]. This essentially means that with diffused junction solar cell it is not possible to achieve the thermodynamic efficiency limit of solar cell. Also, in the diffused junction the use of thin wafers (< 50 um) are problematic because of the requirement of high temperature processing steps. But a number of roadmaps have identified solar cells manufactured only on thinner silicon wafers to achieve lower cost and higher efficiency[3]

An alternative to diffused junction technology is the silicon heterostructure solar cells. In this technology, thin films of amorphous materials are deposited on silicon substrate and the active junction p-n junction is induced in crystalline silicon. As, the junction is formed without the application of extrinsic doping, the devices have a low emitter recombination current resulting in a high open circuit voltage. In fact, the highest V_{oc} of silicon based solar cell is obtained with Sanyo's heterojunction solar cell which is based on silicon heterostructure technology with a-Si as the deposited thin film[4]. Also, the low temperature deposition makes possible the usage of ultra-thin silicon. The most dominant of silicon based heterostructure is the a-Si/c-Si heterojunction technology and the thesis will focus on this particular type of silicon heterostructure technology. But the observations and explanations can be extended to any other silicon heterostructure technology. A schematic of conventional front/rear contact a-Si/c-Si heterojunction is sketched in Figure 1. Thin films (in order of nanometers) of amorphous silicon (a-Si) are deposited on both sides of crystalline silicon (c-Si) substrate. The a-Si layers are followed by sputter deposited transparent conducting oxide (on single side or both sides) and metal contacts[4].

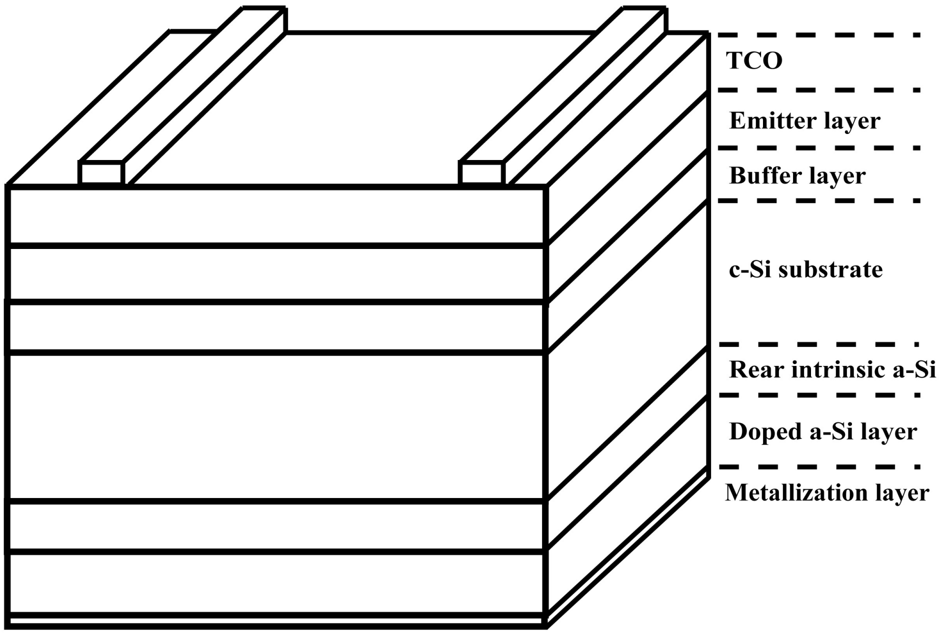

Figure 1. Schematic diagram of a-Si/c-Si heterojunction solar cell.

The first a-Si/c-Si heterojunction solar cell was fabricated without the intrinsic layer [5]but afterwards it was found that the addition of the intrinsic layer increases the V_{oc} and the overall efficiency. But in recent time it has been reported, particularly for a-Si/c-Si heterojunction devices with both contacts on the rear that the addition of intrinsic layer decreases the fill factor [6]. An obvious explanation of the observation is not reported in literature. It is a fact that although a-Si/c-Si heterojunction is under mass production and has reported high efficiency (~ 23 %), a detailed working principles of the devices are poorly understood. In this thesis, a novel theory describing the operation of a-Si/c-Si heterojunction will be proposed and experimentally established. The theory will help in understanding the role of the properties of a-Si layers and interface between a-Si and c-Si in affecting the device performance, particularly the minority carrier transport mechanism.

The thermodynamic limit of photovoltaic conversion is about 80 %. But single junction solar cells based on silicon heterostructure can only achieve efficiencies of 31 %. A number of approaches have been proposed to close the gap between the thermodynamic limit and that commonly achieved by single junction solar cells. A heterodevice with nanostructured absorbing medium is one of the concepts. In this concept, the existence of MQFL allows the absorption of sub-band gap photons but the current is delivered at a voltage defined by the higher band gap material[7]. Both quantum well and quantum dot can be used to realize the nanostructured absorbing medium. In this thesis, the material combinations that can realize a MQFL system in quantum well structure is identified and the absorption coefficient of one of the combination is calculated. The thesis discusses the growth of GaAsSb layer, as GaAsSb(barrier)/ InAs(dot) has been identified in a previous work to be a candidate material for quantum dot structure.

1.2 Dissertation outline

Chapter 1 describes the computer modeling of c-Si based heterostructure, with a particular emphasis on a-Si/c-Si heterojunction solar cell. The computer model is developed in the commercial simulator, Sentaurus. The model allows the inclusion of user defined defect states in a-Si, tunneling of carriers at the heterointerface and optical generation. The experimental results are then compared with the simulated results to validate the computer model.

The band diagram analysis of a-Si/c-Si heterojunction solar cell is performed in Chapter 2. The band diagram is obtained with the computer model described in Chapter 1. The simulated band diagram shows the presence of an inversion region at the interface between a-Si and c-Si (heterointerface) on the crystalline silicon side. The presence of inversion region is experimentally corroborated by lateral conductance measurement. The presence of inversion region implies strong band bending near the heterointerface. The band bending influences the effective barrier the photocarriers face at the heterointerface, thereby affecting the minority carrier transport mechanism.

The influence of band bending in affecting the transport mechanism is studied in Chapter 3. The chapter provides theoretical calculations that correlate band bending with minority carrier transport mechanism. The results show that a stronger band bending assists in the transport mechanism. In chapter 4, the effect of device parameters in the performance of a-Si/c-Si heterojunction solar cell is discussed. The results show that the band offset at the interface between a-Si and c-Si, the intrinsic layer thickness, emitter layer doping and heterointerface affects the fill factor and hence the performance of a-Si/c-Si heterojunction solar cell.

Chapter 6 proposes a novel theory explaining the operation of a-Si/c-Si heterojunction solar cell. The role of the constituent a-Si layers are defined in context of the theory. A novel device structure named ‘Selective carrier contact device’ is outlined and based on theoretical calculations it is shown that the device has the potential to achieve the maximum theoretical efficiency of silicon based heterostructure.

Chapter 7 describes an experimental technique to extract the recombination parameters of a-Si/c-Si heterojunction solar cell. The methodology relies on measuring the inverse lifetime by Sinton lifetime tester and fitting the experimental data with polynomial of appropriate order.

In chapter 8, the material combinations that can be used in a quantum well solar cell to realize a multiple quasi-fermi level will be discussed. The calculations are performed on different possible combinations of direct band gap III-V semiconductors with the effect of strain being taken into account by applying 6 band k•p model. A detailed balance calculation is also done on the materials selected to determine their maximum efficiency under black body radiation.

The absorption coefficient of a MQFL system is calculated in Chapter 9. The absorption coefficient of one of the transition (transition from valence band to confined state in the quantum well) for a MQFL system is derived from Fermi's golden rule while the other two absorption coefficients are calculated based on previously published work. The results are discussed with respect to AlInAs (barrier)/ InAsP (well) material combination which have been identified in the previous chapter to be a candidate for MQFL system.

In chapter 10, the growth mechanism of epitaxial layers of GaAsSb by molecular beam epitaxy on GaAs (001) substrates with the Sb/As flux ratio varied for growth temperatures of 470 C, 500 C and 530 C is discussed. The compositions of the layers are determined by high resolution X-ray diffraction. The results are analyzed using a non-equilibrium thermodynamic model of the epitaxial growth of strained III-V-V compounds with the Sb/As equilibrium flux ratio as a fitting parameter.

The effect of Sb/As soak times prior to growth of GaAsSb on GaAs are investigated by X-Ray Diffraction and Photoluminescence (PL) in Chapter 11. Multiple quantum well samples with soak times of 0s, 30s, 60s are grown at 500C with nominally identical Sb and As fluxes to determine the optimum soak time.

Chapter 2

MODELING OF AMORPHOUS SILICON/CRYSTALLINE SILICON HETEROJUNCTION SOLAR CELLS

2.1 Introduction

A predictive computer model is indispensable in understanding the device characteristics and operation. Chapter 2 of the thesis is focused on developing a computer model of the amorphous silicon/crystalline silicon (a-Si/c-Si) heterojunction solar cell. Previously, computer models based in programs such as PC1D, AFORS-HET and AMPS-1D have been used but suffer from drawbacks such as not including the option of modeling the gap states in a-Si and the tunneling at the interface between a-Si and c-Si (heterointerface) and in the bulk of a-Si[8,9]. These shortcomings can hinder the proper modeling of a-Si/c-Si heterojunction solar cells. The defects in amorphous silicon (a-Si) and at the heterointerface between c-Si and a-Si plays an important role in defining the device characteristics and the tunneling mechanisms at the heterointerface has been proposed[10] to be a major physical mechanism occurring in the device. So, in this chapter, the commercial software package Sentaurus has been used to develop the computer model. Section 2.2 outlines the computer model while section 2.3 compares the experimental results with simulated results.

2.2 Computer model of a-Si/c-Si heterojunction

Sentaurus is used as the basis for the a-Si/c-Si heterojunction model for several reasons, including; allowing accurate models of defects in bulk materials and the ability to modify the defect models with user defined programs to approximate a-Si material. Sentaurus solves the charge transport based on the Poisson equation and the electron and hole continuity equations. The drift-diffusion model has been used for modeling the transport mechanism in the bulk of a-Si/c-Si heterojunction. The carriers are modeled to cross the heterointerface by thermionic emission and tunneling mechanism. The coefficients and the boundary conditions of equations are determined by factors such as the generation and recombination rates, the mobility, the interface and boundary conditions at the contact. An accurate Sentaurus model requires a model (consisting of specifying the material parameters and physical mechanism) for the a-Si, for the c-Si, and specifying the physical processes at the interface. The paragraphs below give a description of the parameter values and the physical mechanisms occurring in each region.

The material parameters for c-Si used in the simulation (except the bulk lifetime which is specified by the user to accommodate different materials and structures), are the default values used by Sentaurus. The crystalline silicon is used as the base of the solar cell and is lightly doped ($\sim 10^{15}/cm^3$). The bulk lifetime for n-doped float zone crystalline silicon has been found to be greater than 3 ms[11] and even as high as 35 ms[12]. A value of 5 ms for the bulk lifetime is used for the simulations. Because of the low doping in these simulations, band gap narrowing has been neglected. Both Auger recombination and Shockley-Read-Hall (SRH) recombination are included. Auger recombination coefficients are dependent on both carrier injection and temperature[13,14]. For SRH recombination, the lifetime has been taken equal to the bulk lifetime and a single defect level has been considered at the mid-gap.

The modeling of a-Si in Sentaurus is less well-developed than a bulk semiconductor. Sentaurus models only a single band gap for a particular material, and for modeling a-Si, it had been assumed that the optical band gap is equal to the mobility gap[15]. The band gap is taken to be 1.72 eV for intrinsic a-Si, consistent with our experimental data. The electron affinity for a-Si is set at 3.9 eV while for c-Si it is 4.05 eV[16]. Since Sentaurus follows Anderson's model of band alignment at the heterointerface, this gives a conduction band offset of 0.15 eV and valence band offset of 0.45 eV, which is consistent with the values reported in literature[17]. The defects in amorphous silicon can be divided into two types; band tail states and dangling bond states. The band tail states have been modeled as an exponential distribution of acceptor-type defects for the conduction band tail and donor-type defects for the valence band tail. The slope of the tail is taken to be 45 meV[18] for valence band tail and 25 meV[19] for conduction band tail with the peak concentration equal to the effective density of states. The dangling bond states are modeled based on "defect pool" model. The defect pool model states that the dangling bond distribution is dependent on the position of the Fermi level and hence on the doping in a-Si[20]. A code was written in MATLAB which calculates the dangling bond distribution based on the type and level of doping in a-Si as well as on other parameters such as the width of the defect pool, and the most probable energy of defect formation. To incorporate the effect that the dangling bond states do not follow Fermi-Dirac statistics, the defect state distribution was converted to a one electron density of state by applying the transformation as described in literature [20] . A two column table containing the energy and defect density is generated in MATLAB and is used in Sentaurus to define the dangling bond state distribution for a-Si. The trap definition is completed by specifying the electron and hole capture cross-sections. The capture cross-section for electrons and holes in a-Si are noted to vary from 1×10^{-18} cm^2 to 1×10^{-15} cm^2 [21] and from 1×10^{-17} cm^2 to 8×10^{-15} cm^2 [22,23] respectively. The electron and hole capture cross section for acceptor-donor type of defects is set at 10^{-16} cm^2, and 7×10^{-16} cm^2 is taken for the dangling bond states. Also, to accommodate the fact that the capture cross section of charged states and neutral states are different[24], Poole-Frenkel effect is included. The defects in a-Si have an important role in defining the recombination mechanisms occurring in a-Si. The band tail states are acceptor-donor type defects and hence defined by SRH recombination. The situation is different for dangling bond states. The dangling bonds are amphoteric in nature and hence recombination at dangling bonds is not defined by SRH recombination statistics[25]. But since, in this model, the dangling bond state distribution has been converted to one electron density of state, SRH recombination statistics can be applied. Consequently, SRH recombination is used for a-Si. The mobility of carriers is assumed to be constant and taken to be 1 cm^2/Vs and 5 cm^2/Vs for holes and electrons respectively which are close to the values of 0.3 cm^2/Vs and 2 cm^2/Vs[26], being reported in literature for holes and electrons respectively.

The final model needed in Sentaurus is that for the interface. At the interface between a-Si and c-Si, the surface defect states originate both due to the loss of crystalline geometry and also because of deposition of a-Si and other fabrication requirements. The surface states have the following properties, a) they are charge storage centers, b) recombination-generation centers and c) provide additional tunneling path between the interface and the bulk materials[27]. In this work, the interface defect states are described by a single defect level at the mid-gap[28]. Both acceptor-type and donor-type defect is considered for the simulation. It should be mentioned that only the concentration of acceptor-type defect states affect the device performance for p-doped c-Si substrate and vice-versa. In a-Si/c-Si, the surface of c-Si is strongly inverted under ideal operating condition. At and near the interface, the electron concentration (hole concentration) is nearly constant and much higher than the hole concentration (electron concentration) throughout the operating region of the device with p-doped silicon (n-doped silicon). The quasi-Fermi levels at the heterointerface do not cross the mid-level defect states with change in bias[28]. Hence, the occupation probability of defect states is nearly constant throughout the operating region of the device. The recombination-generation properties of surface states are incorporated in the model by surface recombination velocity (SRV), S_n and S_p for the interface between c-Si and a-Si. The SRV, S_n (S_p) is related to the defect concentration by,

$$S_n(S_p) = \sigma_n(\sigma_p)\vartheta_{th}N_{it}$$

where ,σ_n (σ_p) is the capture cross-section, ϑ_{th} is the thermal velocity and N_{it} is the number of interface available interface traps[29]. Since the occupancy of traps is nearly constant at the heterointerface, S_n and S_p is taken to be constant at all biases. The values of S_n and S_p are determined by fitting the theoretical curve with experimental curve. The capture cross-section of electrons and holes for the defect states has been taken to be 5 x 10^{-18} cm^2 and 1 x 10^{-16} cm^2 respectively. The charge originating due to the defect states is calculated by the simulator based on the type of defect state, the concentration and occupancy of the states. To describe the tunneling at the heterointerface, Sentaurus's non-local tunneling model have been used. The model uses four fitting parameters, the tunneling masses, m_c and m_v and the effective Richardson's constant, g_c and g_v. Thus, g_c, g_v , m_c and m_v have been used as the fitting parameter and their value is determined by fitting with the experimental data.

2.3 Comparison of experimental curve with simulated curve

The results of the computer model are compared with the experimental results in this section. The structure chosen for comparison is one with an n-doped crystalline silicon substrate and p doped a-Si layer on the front and n-doped a-Si layer on the rear. The substrate is 300 um with a doping level of 1.88 x10^{15}/ cm^3 while the p a-Si and n a-Si layers are 10 nm each. The structure is similar to the conventional heterojunction solar cell[30] with the only exception of an intrinsic layer in between the c-Si and doped a-Si. In heterojunction solar cell, the intrinsic layer is inserted to obtain a higher open circuit voltage[31] and since the objective of this work is the modeling of a-Si/c-Si heterojunction structure, this structure was considered sufficient for the comparison of the computer model with the experimental results.

Two sets of experimental data are available for the heterojunction structure. One is the current-voltage relationship while the other one is the plot of the minority carrier concentration against the lifetime. The simulated current-voltage relationship is first fitted with the experimental results by changing the interface parameters like the defect density and the tunneling parameters (g_c, g_v , m_c and m_v, S_n and S_p) and the result is given in Figure 2. It is observed while fitting the curves that the acceptor type defects has no effect in the performance of the device. The defect density of the acceptor type defect has been taken to be 1 x 10^{11} / cm^2.

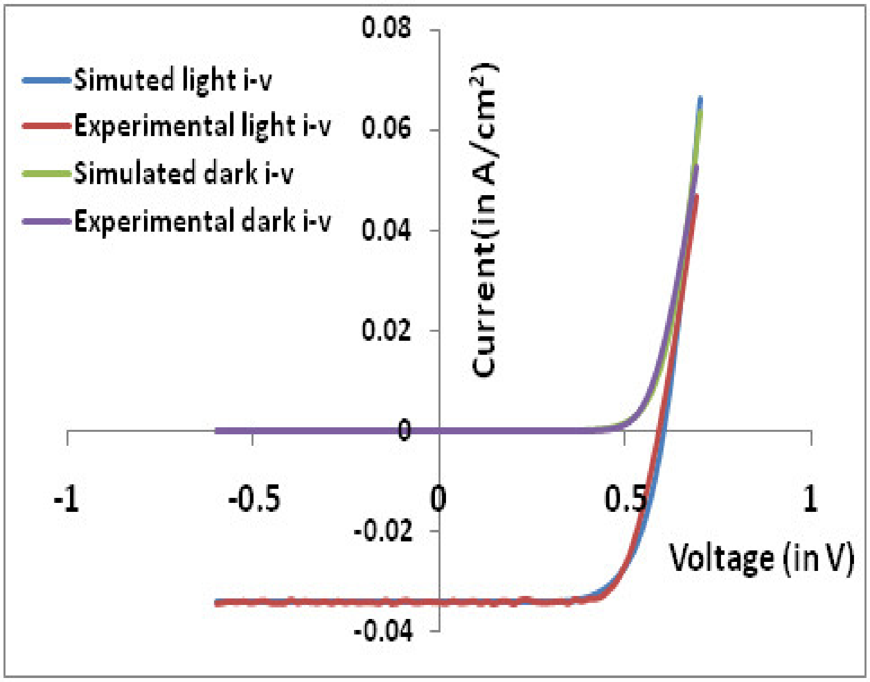

Figure 2. Simulated and experimental current-voltage curve

It should be mentioned that the values as obtained after fitting is not unique but the simulated minority carrier vs. lifetime relationship obtained with the parameter values as mentioned and section 2.2, should have a qualitative fit with the experimental data. The experimental minority carrier vs. lifetime curve is obtained from Sinton Lifetime tester. The lifetime tester uses the optical constant as one of the user defined values. The optical constant for this set of experiment has been taken to be 0.86, which is the short circuit current divided by 38 mA/cm^2, for which the optical constant is 1[32]. The simulated lifetime vs. minority carrier concentration is obtained by dividing the average minority carrier concentration by the total optical generation rate at the open circuit condition taken at different light intensities. The simulated and the experimental curves for minority carrier concentration are shown in Figure 3.

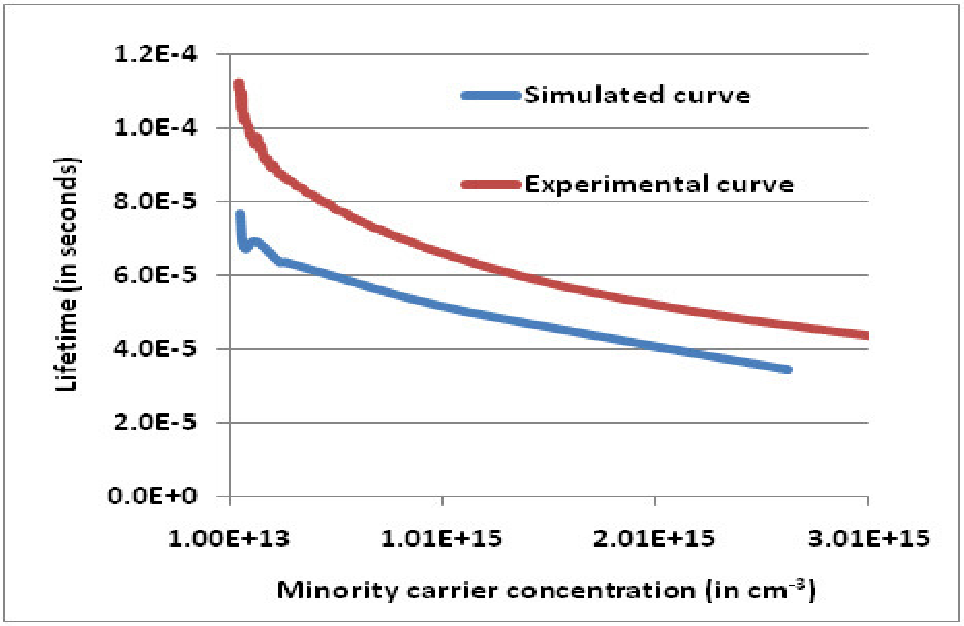

Figure 3. Lifetime curves

2.4 Conclusion

The chapter described the computer model of a-Si/c-Si heterojunction solar cells. The subtle features of the model include the modeling of dangling bond states by defect pool model, the inclusion of Poole Frenkel effect to take into account the change in capture cross-section of charged defects states and the tunneling at the heterointerface. The experimental curves and the simulated curves show a close qualitative fit, thus verifying the validity of the model in predicting the device characteristics of a-Si/c-Si heterojunction. The computer model will be used in later chapters to simulate device characteristic and better understand the operation of a-Si/c-Si heterojunction solar cell.

Chapter 3

BAND DIAGRAM ANALYSIS OF AMORPHOUS SILICON/CRYSTALLINE SILICON HETEROJUNCTION SOLAR CELL

3.1 Introduction

The band diagram of a-Si/c-Si heterojunction solar cell is studied in the chapter. An analysis of band diagram is considered necessary to explain the contradictory events of a high photo-carrier collection probability in a-Si/c-Si heterojunction solar cell, inspite of a large band offset negatively affecting the transport of minority carriers. In the chapter, the band diagram is simulated for the device structure described in Section 3.2 with the computer model outlined in chapter 2. The theoretical analysis is corroborated experimentally by lateral conductance measurement technique.

3.2 Device structure

The schematic of the device structure is sketched in Figure 1. The substrate is single sided polished (top side) p-doped c-Si with a thickness of 675 um and a resistivity of 8-12 ohm-cm. The emitter layer on the top is n^+- doped a-Si with a thickness of 100 nm while the doped layer on the rear is a 10 nm thick p^+ doped a-Si. The intrinsic a-Si layers are each of 7 nm thickness. The a-Si layers are deposited in a PECVD system. From here on any discussion of the intrinsic layer, if not otherwise mentioned will mean the intrinsic layer on the front. On the front, a TLM pattern is created by evaporating a 200 nm of aluminum through a shadow mask. The width of each grid line is approximately 500 um while the grid spacing is 1150 um, 2670 um and 3760 um as measured by an optical microscope.

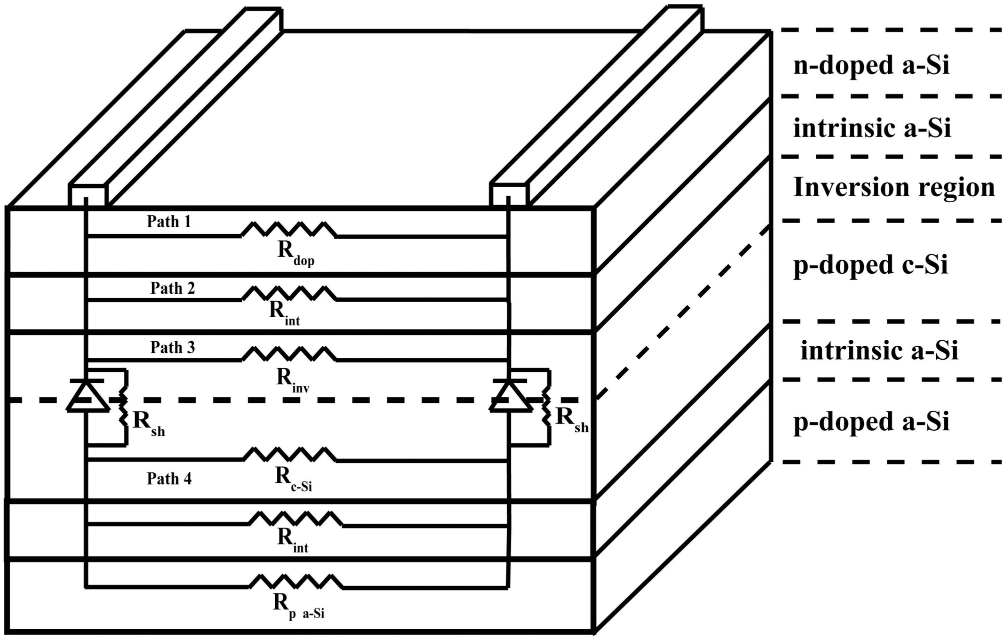

Figure 4. Schematic device structure of a-Si/c-Si heterojunction used for the study. The probable current paths through the device are also sketched.

3.3 Results

The theoretical analysis is performed with a computer model described in Chapter 2.The band diagram under thermal equilibrium obtained by using the described computer model for device structure (Figure 1) is shown in Figure 5. The horizontal axis of Figure 5, plotted in logarithmic scale is the distance from the top along the vertical direction of Figure 1. The band diagram shows that near the heterointerface on the c-Si side, the c-Si has undergone a strong band bending resulting in a type inversion of c-Si at the heterointerface. The active junction is formed inside the bulk of c-Si. In Figure 4, when a voltage difference is applied between the contacts, the current can flow along one of the four alternative paths. The current paths through the n^+-doped a-Si and intrinsic a-Si are mentioned by Path 1 and Path 2 respectively. The current flow through the bulk of c-Si (Path 4) is determined by two back to back diodes. The resistance for Path 4 is infinite for ideal diodes but for real diodes the overall resistance is given by the shunt resistance of the reverse biased diode (R_{sh}) in series with the bulk resistance of c-Si ($R_{c\text{-}Si}$). Being in parallel with $R_{c\text{-}Si}$, the resistances through the intrinsic a-Si and p^+-doped a-Si on the rear have no effect on the overall resistance of Path 4. Path 3 for current flow is due to the presence of an inversion region at the heterointerface and the resistance of the path is determined by the strength of the inversion at the heterointerface.

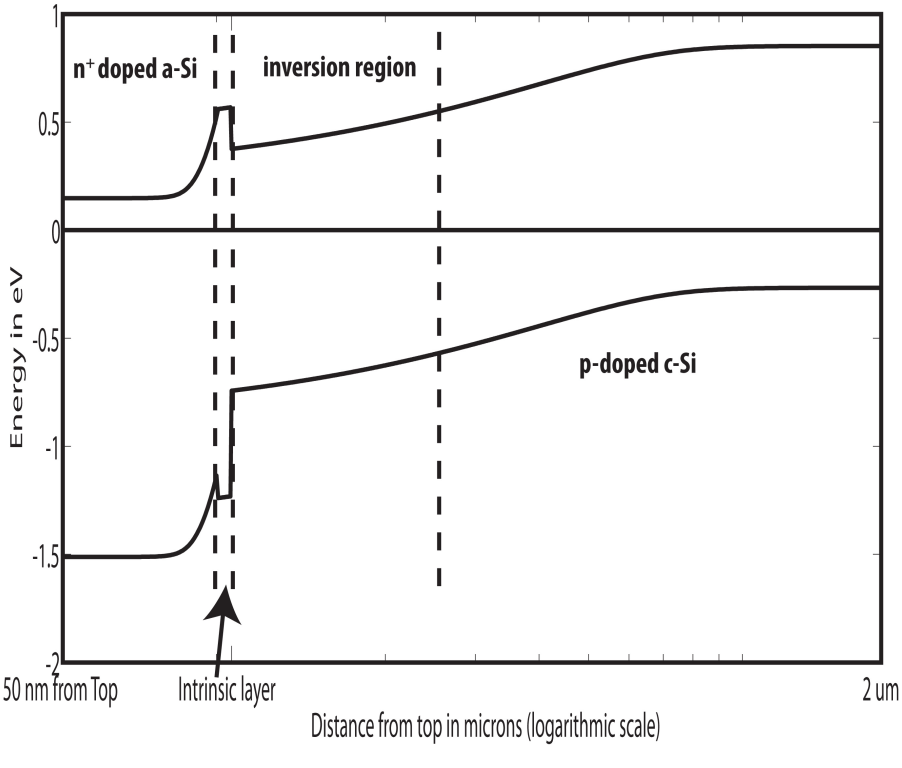

Figure 5. Band diagram under thermal equilibrium for a-Si/c-Si heterojunction. The band diagram shows the inversion region at the interface between a-Si and c-Si.

The overall resistance (R_{tot}) between the contacts is the parallel combination of resistances of the individual paths. The value of R_{tot} is determined by sweeping the voltage from -0.5 V to 0.5 V and measuring the current by using a HP 4145A Semiconductor Parameter Analyzer. The semiconductor chuck is insulated from the p^+-doped a-Si on the rear by placing an insulating material (a thin piece of paper) in between them. The current voltage relationship for each of the grid spacing is linear. The sheet resistance and contact resistance determined from TLM pattern are 13.7 kilo-ohm/sq and 0.11 ohm-cm^2.

R_{dop} is the resistance of the current path through n^+ doped a-Si. R_{dop} is determined separately by using a sample with 100 nm of n^+ doped a-Si deposited on a glass substrate. The contact to the n^+ doped a-Si layer is made by painting two silver lines with approximate length of 25 mm and spacing of 1.5 mm. The sheet resistance obtained for the sample is 6 x 10^7 ohm/sq. R_{int} corresponds to the resistance of the intrinsic layer. Although a study of the band diagram shows that n-type characteristic has been induced in the intrinsic layer, it can be assumed that the resistance of the intrinsic layer is not lower than the n^+- doped a-Si layer. R_{sh} for Path 4 is measured separately by studying the current-voltage relationship under reverse bias of a smaller piece (~ 1 cm^2) of the sample with both front and rear covered completely with aluminum of thicknesses 200 nm and 50 nm respectively. The value of R_{sh} determined is 216 kilo-ohm-cm^2 and the value is in agreement with an implied V_{oc} of 690 mV at 1 sun obtained for the sample without any metallization layers by using Sinton lifetime tester. The contribution of $R_{c\text{-}Si}$ to the resistance of Path 4 can be neglected as it is in series with R_{sh}. The resistances of paths 1, 2 and 4 do not agree with R_{tot}. The value of R_{tot} can be justified by the presence of a high conductance inversion region at the heterointerface as indicated by the band diagram. The simulations performed with the computer model show that for the inversion region to have a sheet resistance of 13.7 kilo-ohm/sq, the Fermi level in n^+-doped a-Si needs to be 0.15 eV from the conduction band edge. The activation energy, which is the separation of Fermi level from band edge in a-Si varies from 1.0 eV in intrinsic a-Si to 0.1 eV in n^+-doped a-Si[33] and so the value of 0.15 eV is in agreement with the range of experimentally observed values.

3.4 Conclusion

The band diagram analysis performed in the chapter shows the existence of an inversion region in a-Si/c-Si heterojunction solar cells at the heterointerface with the active junction being formed inside the c-Si. The lateral conductance measurement is performed to corroborate the theoretical results and a value of 13.7 kilo-ohm/sq is obtained for the sheet resistance. The value is order of magnitude lower than the resistances of the current paths through the n^+ doped a-Si, intrinsic a-Si and the bulk c-Si. The result can be explained only by the presence of an inversion region at the heterointerface. The inversion region provides a parallel path to the flow of current and because of the high conductivity, the conduction mechanism primarily occurs through the inversion region and hence, the overall resistance depends on the sheet resistance of the inversion region. The presence of the inversion region near the heterointerface affects the effective barrier to the minority carrier transport .The next chapter will study the effect of the band bending in the minority carrier transport mechanism across the buffer layer.

Chapter 4

EFFECT OF BAND BENDING AT THE HETEROINTERFACE IN THE TRANSPORT OF MINORITY CARRIERS

4.1 Introduction

Chapter 4 models the transport mechanism, calculates the rate of transition of minority carriers across the buffer layer and explains the role of band bending in influencing the transport mechanisms. Section 4.2 describes the theoretical background for the calculation of the rate of transition of minority carriers across the buffer layer. The transport mechanisms considered are iso-energetic hopping, Poole-Frenkel emission and capture and emission of a carrier by the defect state at the same energy level. Section 4.3 describes the methodology for the calculation of the rate of transition. The electric field and band energies required for the calculation of the transition rates are obtained by the solution of the drift-diffusion model (DD model) developed in the commercial simulator Sentaurus. The rates of transitions are calculated in a post-processing scheme by using the solution of the DD model (electric field and band energy) and the relationships discussed in section 4.2. In section 4.4, the calculations are performed under two different conditions of band bending; strongly inverted and weakly inverted c-Si surface at the heterointerface. Section 4.5 concludes the paper.

4.2 Theory

The device structure is similar to Figure 1. In the chapter, if not otherwise mentioned, the a-Si layers are 10 nm in thickness. The emitter layer is p-doped while the c-Si is n-doped of thickness 200 microns. The work focuses on explaining the transport mechanisms across the buffer layer and hence the TCO and metallization layers are not included in the model and an ideal ohmic contact to the doped a-Si:H layers are assumed. The band diagram under thermal equilibrium of a-Si/c-Si heterojunction solar cell (Figure 1) is sketched in Figure 6. The band diagram is obtained by a computer model described in Chapter 2. The band diagram is plotted to a thickness of 2 microns from top of the structure. Under illumination, the absorption of photons primarily occurs in the c-Si. Although a small fraction of the photocurrent in a-Si/c-Si heterojunction solar cell is due to the absorption of photons, the work will only concentrate on the photogenerated minority carriers in c-Si. The minority carriers have to cross the buffer layer before getting collected as majority carriers. In this work, it will be assumed that the carriers are collected as majority carriers once they reach the emitter or the extended states of the buffer layer. The potential variation across the buffer layer is assumed to be linear. The heavily doped a-Si emitter layer is taken equivalent to a metal layer, with the difference between majority carrier quasi-Fermi level and vacuum analogous to work-function of the metal. Under the stated assumptions, the minority carriers will face a trapezoidal or triangular barrier at the heterointerface before being collected as majority carriers. The slope of the potential variation, thickness of buffer layer and band offset at the heterointerface will determine whether the shape is triangular or trapezoidal.

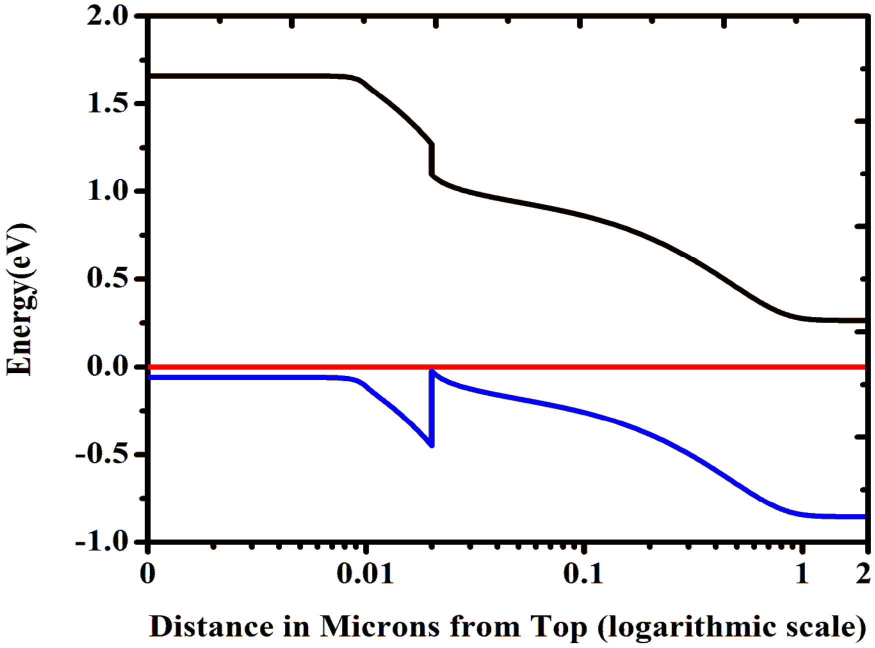

Figure 6. Band diagram at thermal equilibrium for a-Si/c-Si heterojunction solar cell. The band diagram is sketched to a thickness of 2 microns from the top.

The transport mechanisms of minority carriers across the buffer layer that are considered in this work are outlined in Figure 7. Mechanism 2 corresponds to iso-energetic hopping or trap-assisted tunneling. The calculation of rate of transition for mechanism 2 requires a detailed knowledge of the distribution of trap states in the buffer layer. The defect states in the buffer layer (intrinsic a-Si) consists of two exponential tail states, one each of an acceptor and a donor type defect and Gaussian mid-gap states of dangling bonds. In high quality intrinsic a-Si, the density of mid-gap states is much lower than the exponential tail state density[15] and is neglected in calculating the transition rate in this work. Based on the band diagram, it can be inferred that only the valence band tail states will participate in the transport mechanism marked 2 in Figure 7. Also, in this work it is assumed that the valence band tail states above the hole quasi-Fermi level is occupied with holes and hence unable to participate in the transport while the valence band tail states below the hole quasi-Fermi level is empty and capable of participating in the transport. The exponential tail trap density varies as,

$$N=N_o \exp\left(-\frac{E}{E_{vt}}\right)$$

Where, N_0 is the peak trap density, E is the energy from band edge and E_{vt} is the characteristic band tail state energy. A value of $2 \times 10^{20}/cm^3$ and 45 meV[34] is taken for N_o and E_{vt} respectively. The barrier (valence band offset) is divided into intervals of 25 meV. The total number of traps within the energy interval is calculated by integrating within that interval. Due to trapezoidal nature of the barrier, trap density at a fixed energy, E, with respect to the valence band edge will vary along the tunneling path. To overcome this difficulty, an average trap density has been used in the calculation and is given by,

$$N_{avg}(E)=\frac{1}{d_{max}} * \int_0^{dmax} N(x,E)dx$$

d_{max} is the distance carriers need to travel at a particular energy before being collected as majority carriers. The rate of transition from a defect state to another defect state is[35,36],

$$R = \vartheta * \frac{N_{avg}(E)}{N_{i,tot}} * \exp\left(-\frac{r_{i,tot}}{2R_o}\right)$$

where, ϑ is an attempt-to-hop frequency, $N_{i,tot} \approx \sum_k N_{avg}(E_k), k \geq i$, is the total number of iso-energetic and deeper sites with corresponding mean separation, $r_{i,tot} = (N_{i,tot})^{-1/3}$ and R_o is a localization parameter for the sites. The value of R_o is 5×10^{-8} in this work [35]. A hole trapped inside a defect state escape by mechanism

3 to get collected as majority carriers. The rate of transition for mechanism 3 is given by,

$$R3 = \vartheta * P_{def}$$

where, ϑ is attempt-to-escape frequency and P_{def} is the tunneling probability. The tunneling probability is obtained from WKB approximation and is given by,

$$P_{def}=\exp(-2\int_{x1}^{x2} k(x)dx)$$

where, x_1 and x_2 are the initial and final position and k(x) is the position dependent wave-vector. The trapped holes can escape from defect states by Poole-Frenkel emission (mechanism 4) into the valence band with rate,

$$R_{PF}=\vartheta * \exp\left(-\frac{E_D}{kT}\right)\{\frac{1}{\beta^2}(1+\left(\beta-1\right)\exp(\beta)+\frac{1}{2}\}$$

The rate of transition for mechanism 1 is given by,

$$R1=C_1(E)P_{tun}(E)f(E)$$

where, $P_{tun}(E)$ is the tunneling probability calculated in the same way as for mechanism 3 and f(E) is the probability that the state is empty. f(E) is equal to unity in this work. $C_1(E)$ is the number of carriers impinging on the heterointerface at a particular energy level.

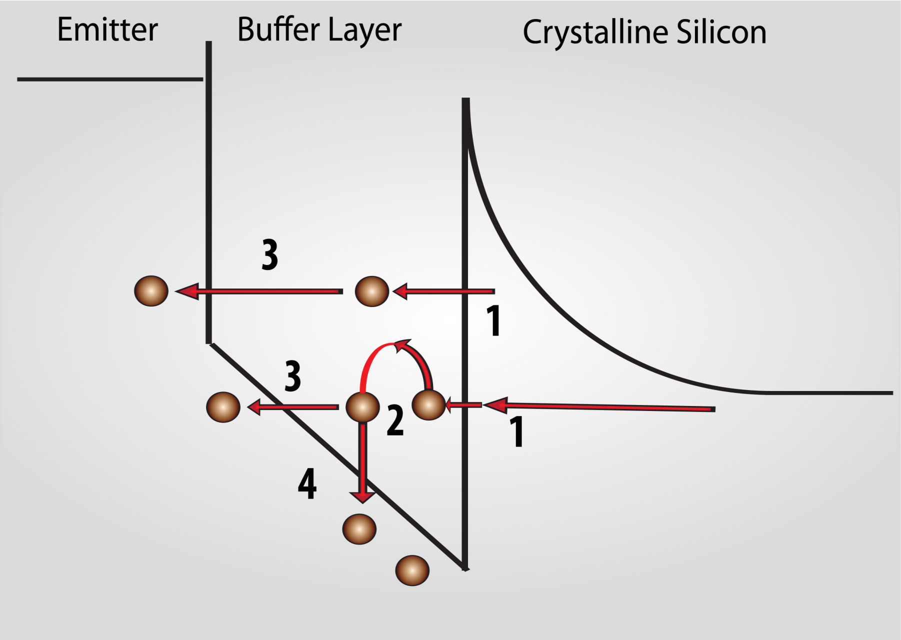

Figure 7. Transport mechanisms across the buffer layer. 1: Capture of a carrier by a defect state. 2: Iso-energetic or trap-assisted tunneling. 3: Emission of a carrier by a defect state 4: Poole-Frenkel emission.

4.3 Methodology

The calculation of the rate of transition of minority carriers across the buffer layer requires a precise quantitative knowledge of the valence band energy and the electric field near the heterointerface. The value of the electric field and the VBE is obtained by a solution of a-Si/c-Si heterojunction solar cell at a particular voltage with a computer model using drift-diffusion transport equation developed in the commercial simulator Sentaurus. In devices with strongly inverted c-Si near the heterointerface, the band bending is independent of the applied bias but the same is not true for devices without the inversion layer. So, a voltage of 0.6 V is chosen for the calculation as it is close to the maximum operating point of a-Si/c-Si heterojunction solar cell. A study of the electric field shows that under certain conditions of band bending, the value can exceed 50 kV/cm. The distribution of minority carriers reaching the heterointerface after traversing through such an extremely high electric field cannot be described by a thermal population and hence the calculation of C_1 (the carriers impinging on the heterointerface) based on Maxwellian distribution of carriers is not valid[37]. In order to overcome the problem and include the effect of electric field in affecting the distribution of minority carrier population, an ensemble Monte Carlo scheme is used. Based on the electric field obtained from the DD simulator, c-Si is divided into two regions; Region 1 with electric field less than 1 kV/cm and Region 2 with electric field greater than or equal to 1 kV/cm. It is assumed that the carrier population in Region 1 can be described by a Maxwellian distribution and the solution of the drift-diffusion equation is valid. In order to simulate the transport of minority carriers in region 2, an ensemble Monte Carlo (MC) technique is used. An ensemble MC is based on initializing a statistically large number of carriers and simulating their motion through the crystal lattice under the applied electric field (known as free flight), with the free flight terminated by instantaneous scattering event. The MC algorithm consists; 1) Generating free flight times for each particle based on a random number generated and letting the carrier drift for the free flight time under the applied electric field, 2) The free flight is terminated by an instantaneous scattering event chosen based on a random number generated, 3) The final momentum and energy of the particle after scattering is assigned depending on the scattering mechanism that is selected, 4) The whole sequence is then repeated for the next free flight[37]. In this work, an ensemble of 25,000 particles is initialized at the interface between region

1 and region 2. The distribution in energy of the ensemble follows Maxwellian distribution. The electric field is obtained from the solution of drift-diffusion solver and it varies along the path of motion of the particle in real space. The electric field is assumed to be present along x-direction and the motion of the particle is simulated along the x-direction of real space only. The MC domain (region 2) is divided into a number of intervals (1-D cells). The electric field assigned to the particle within a particular interval equals the value of the field at mid-point of the interval. The particle's position is updated in real space every 0.2 fs so that the carriers do not move too far from the 1-D cell for which the electric field is assigned to it. In contrary to the standard MC technique, no effort has been made to solve the Poisson's equation over the MC domain after the positions of the particles have been re-assigned[38]. The electric field is assumed to be constant[39] and also no effort has been made to feedback the information obtained from the MC simulation to the drift-diffusion simulator. In the MC region, no recombination-generation event is considered. This is reasonable considering that the MC domain is about 100 nm and the diffusion length of the carriers is in the order of millimeters. The valence band (minority carriers are holes, in this work) for MC simulation is assumed to be one single spherical, parabolic band with an effective mass related to some plausible average in k-space[40]. The scattering mechanism considered are acoustic phonon scattering, optical phonon scattering and ionized impurity scattering. At the end of MC domain which coincides with the heterointerface, the carriers are collected and the distribution of carriers as a function of energy is obtained. The barrier (valence band offset between a-Si and

c-Si) is divided into intervals of kT (25 meV) each. The value of the mid-point denotes each energy interval. C_1 (ΔE) is calculated for the intervals with considering that the integrated current density impinging on the heterointerface to be 40 mA/cm^2.

For each energy interval, 10,000 individual percolation paths are created. The methodology to create the percolation path is mentioned as follows: A set of random numbers between 0 and 1 is generated. The set of random numbers is multiplied by the maximum distance the carriers need to travel at a particular energy to get collected as majority carriers (d_{max}). The product gives the distance the carriers will travel in each path before being captured by a defect. The rate of transition corresponds to mechanism 1 in Figure 7. According to the model, the carriers captured in a defect state have the option of either escaping from that state by tunneling or Poole-Frenkel emission. A set of random numbers are generated to choose between tunneling and PF emission ($0 \leq R_n < 0.5$ correspond to tunneling and $0.5 \leq R_n \leq 1$ corresponds to PF emission, where R_n is the random number). In case of tunneling, if the distance the carriers need to be collected as majority carriers is less than the mean separation ($r_{i,tot}$) between the two defect states, the carrier will follow mechanism 3 or else it follows mechanism 2. The process is continued till all the carriers are collected as majority carriers. The rate of transition along any percolation path is determined by the slowest of all the steps and the rate of transition for each percolation path is taken to be equal to the slowest step[41]. Also, in this work it will be assumed that at a particular energy, the carriers transport through the buffer layer along the path that has the highest rate of transition. So, for each energy interval, the percolation path with the highest rate of transition is chosen and the rate of transition along that path corresponds to the rate of transmission across the barrier for that particular energy. C_{ext} (E), the carriers extracted from the device is given by $C_{ext}(E) = \sigma N(E)R(E)$, where σ is the capture cross-section and equal to 10^{-14} cm^2, N(E) is the number of traps participating and R(E) is the rate of transmission[42]. In cases where $C_{ext}(E)$ is greater than $C_1(E)$, it is taken equal to $C_1(E)$[43].

4.4 Results

The calculations are performed under two different conditions of band bending; a) strongly inverted c-Si surface (Case a) and b) weakly inverted c-Si surface (Case b). In a strongly inverted c-Si surface, the level of p-type doping induced due to band bending at the c-Si surface is higher than the n-type doping in quasi-neutral region while in weakly inverted c-Si, the relative p-type doping is higher than the n-type doping at the c-Si surface but the level of p-doping is less than the n-doping in quasi-neutral region. Figure 8 shows the distribution of minority carriers as a function of energy at the heterointerface as calculated from the MC simulation. The zero of the horizontal axis in the plot corresponds to the edge of the valence band at the c-Si side of the heterointerface. In accordance with the nomenclature used in defining the energy values in the plots in Figure 8 and Figure 9, the energy values away from the valence band edge in the downward direction of the triangular well formed at the heterointerface is defined as higher energy. The calculations are performed to an energy value of 0.45 eV from the valence band edge of c-Si (Valence band offset is 0.45 eV). The marker for the highest energy is at a value of 0.4375 eV, which corresponds to the midpoint of the energy interval from 0.425 eV to 0.45 eV. The plot in Figure 8 shows that for Case a, the distribution of minority carriers is shifted towards higher energy as compared to Case b. The electric field near the heterointerface is stronger in Case a. The minority carriers reaching the heterointerface gains on average a larger amount of energy resulting in a shift of the distribution of minority carriers towards higher energy values in Case a as compared to Case b.

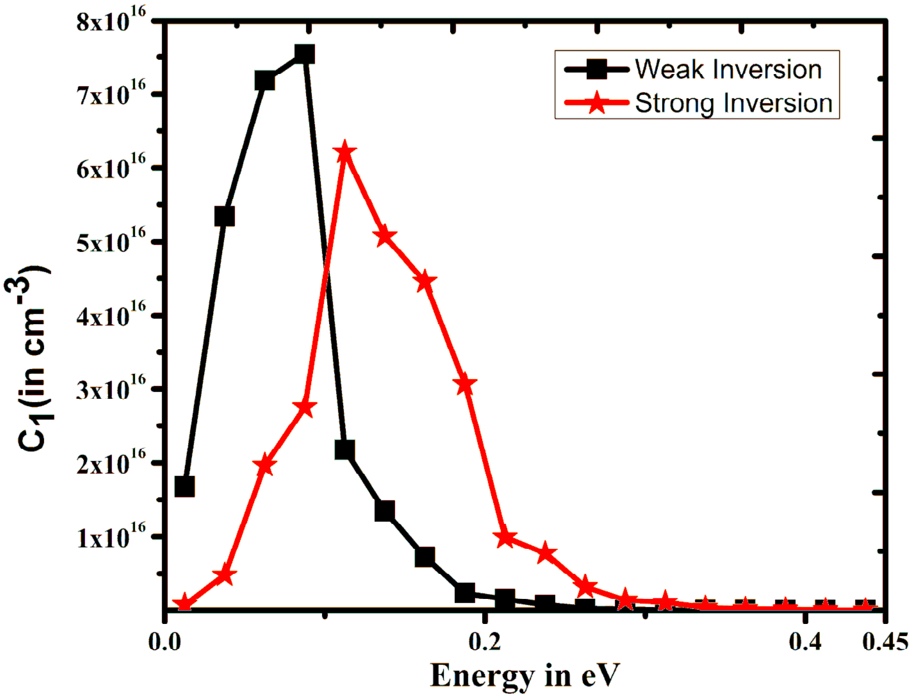

Figure 8. Distribution of injected carriers at the heterointerface. The plot shows that the distribution is shifted towards higher energy values in devices with a stronger inversion.

Figure 9 shows the distribution of collected carrier (C_{ext}) as a function of energy. The plot shows that the total number of carriers (area under the plot) is greater for device with a strong inverted surface than with a weak inversion. A stronger electric field associated with Case a aligns the valence bands of c-Si and a-Si closer and thus the distance the carriers need to traverse through the buffer layer is shorter in Case a. Also, a higher electric field near the heterointerface causes the minority carrier distribution to shift towards higher energy values. As evident from the band diagram, at higher energy values the tunneling distance is shorter and also the number of traps involved in the transport mechanism increases. The two effects are reflected in an overall increase in the total number of carriers that are collected in Case a as compared to Case b.

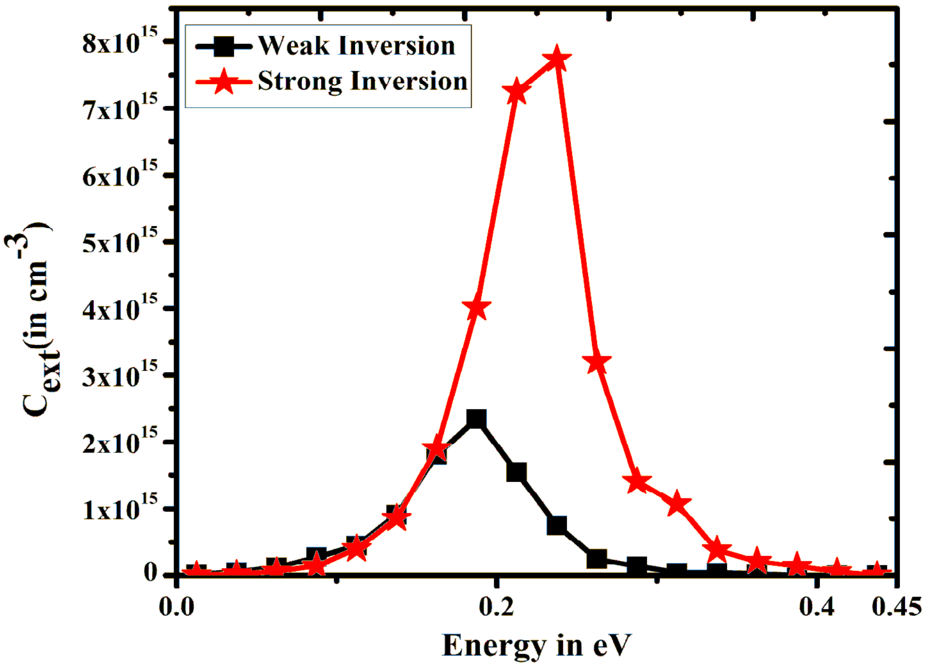

Figure 9. Distribution of extracted carriers at two different conditions of band bending.

4.5 Conclusion

The work explains the role of band bending in the transport mechanism across the buffer layer. The transport mechanisms considered in the modeling are iso-energetic hopping, Poole-Frenkel emission and capture-emission of defect states at the same energy level. A theoretical model that calculates the number of carriers collected at a given band bending condition is developed based on the transport mechanisms. Based on the model, the calculations are performed under different conditions of band bending; strongly inverted and weakly inverted c-Si surface. The calculations show that the total number of carriers collected is higher for a strongly inverted c-Si surface.

Chapter 5

EFFECT OF DEVICE PARAMETERS IN PERFORMANCE OF AMORPHOUS SILICON/ CRYSTALLINE SILICON HETEROJUNCTION

5.1 Introduction

Chapter 4 outlined the effect of band bending in the transport of minority carriers. The results indicate that the transport is assisted by a stronger band bending at the heterointerface. Theoretical study is performed in this chapter to determine the device parameters that influence the band bending at the heterointerface and both simulated and experimental data is provided to study the effect of variation of the parameters in solar cell performance. A set of simulations is also performed to observe the effect of variation of band offset in the performance of a-Si/c-Si heterojunction solar cell and experimental data is provided to corroborate the results.

5.2 Background

The device structure for simulation is similar to Figure 1. In the simulation, the c-Si is n-doped with a thickness of 300 microns. The back surface field is comprised of a combination of intrinsic layer and an n^+ doped a-Si layer with thicknesses of 10 nm each. On the front, a 10 nm p^+ doped a-Si is the emitter of the solar cell. The intrinsic layer on the front between the emitter and c-Si substrate is 7 nm. If not otherwise mentioned, from here on, any mention of the intrinsic layer means the intrinsic a-Si layer on the front. The computer simulation is performed with the model developed in commercial simulator Sentaurus. Apart from the description of dangling bond states in a-Si, the computer model is same as described in Chapter 2. The dangling bond defect states in both n^+ doped and p^+ doped a-Si layers are described by two Gaussian distributions of donor and acceptor type, located at 0.58 eV and 0.78 eV from the valence band edge respectively and with a standard deviation of 0.23 eV. The doping levels, in both a-Si layers are so adjusted that the Fermi level is 0.2 eV from the respective bands (conduction band for n^+ a-Si and vice-versa)[44]. The defect density at the heterointerface is $1 \times 10^{10}/\text{cm}^2$. In cases, where the parameters vary from these values, it will be explicitly mentioned.

5.3 Effect of device parameter on band bending

The band bending at the heterointerface is related to the electric field at the c-Si surface and hence a study is performed in this section to understand the factors affecting the electric field at the c-Si surface. The electric field is related to charge by $\nabla\varepsilon_s.E = \rho(r)$. A plot of the space charge as a function of position is shown in Figure 10.

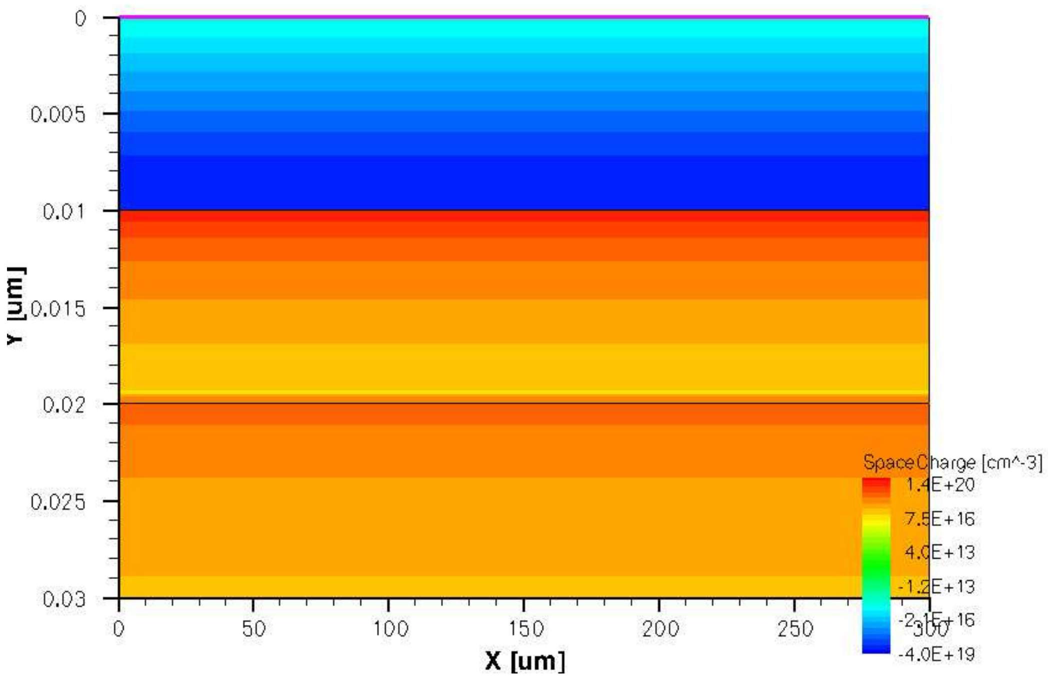

Figure 10. Space Charge at thermal equilibrium

The plot shows that the space charge region is not varying in the direction of the width of the device and hence the relation between electric field and charge for this device can be treated as one-dimensional without the loss of generality. The relationship between charge and electric field for the intrinsic layer of thickness ‘l’ and its beginning at x=0 as seen from Figure 10 can be written as[45],

$$\frac{\partial E}{\partial x} = \frac{1}{\varepsilon_s}\, k(x) \quad 0 < x < l\text{-}\Delta d;$$

$$= \frac{\rho_2}{\varepsilon_s} \quad l - \Delta d \le x \le l$$

In above equation, k(x) is the positive charge density existing in the intrinsic a-Si region. The term ρ_2 denotes the positive charge density at the interface between a-Si and c-Si which arises due to the defect states arising due to different c-Si surface preparation and a-Si deposition conditions. Δd is the spread of the charged states in space. The value of ρ_2 and Δd can be obtained from the plot in Figure 10.

The initial conditions of electric field E_0 and potential, Ψ_o at x=0, is obtained by solving the corresponding equations for electric field and potential in the p-doped a-Si region. The exact solution would require a self-consistent solution of all the corresponding equations but the result can be approximated by assuming that the space charge region is of constant value, ρ_1 and spread over a distance, d_1. The results hence obtained is: $E_o = - \rho_1 d_1/\varepsilon_s$ and $\Psi_o = \rho_1 d_1^2/2\varepsilon_s$. Hence the electric field at the c-Si surface can be related by the equation as follows,

$$E = -\rho_1 d_1/\varepsilon_s + 1/\varepsilon_s \int_0^{l-\Delta d} k(x).dx \;\; + \rho_2 \Delta d/\varepsilon_s$$

The equation shows that the factors affecting the electric field at c-Si surface and hence the band bending at heterointerface are the level of doping in doped a-Si layer, the intrinsic layer thickness(l) and the defect density (ρ_2) at the heterointerface.

5.4 Effect of variation of intrinsic layer thickness

The intrinsic layer thicknesses for simulation are 7 nm, 15 nm, 20 nm and 30 nm. The illumination spectrum for the simulation is the 35 points intensity-wavelength relationship used in PC-1D. The intrinsic layer improves the open circuit voltage by providing excellent surface passivation. By decreasing the thickness of the intrinsic layer it is expected that the surface passivation quality will deteriorate with a corresponding drop in open-circuit voltage but simultaneously a thinner intrinsic a-Si layer will reduce absorption losses, thereby enhancing short-circuit current. In this chapter, the focus of discussion will be to understand the effect of variation of intrinsic layer thickness on the fill factor of a-Si/c-Si heterojunction solar cell. The electric field at the heterointerface under thermal equilibrium and fill factor is shown in Figure 11. The simulated curves for illuminated current-voltage characteristics are shown in Figure 12 while the experimental results showing the effect of variation of intrinsic layer thickness on the performance of heterojunction is obtained from reference and shown below in Figure 13.

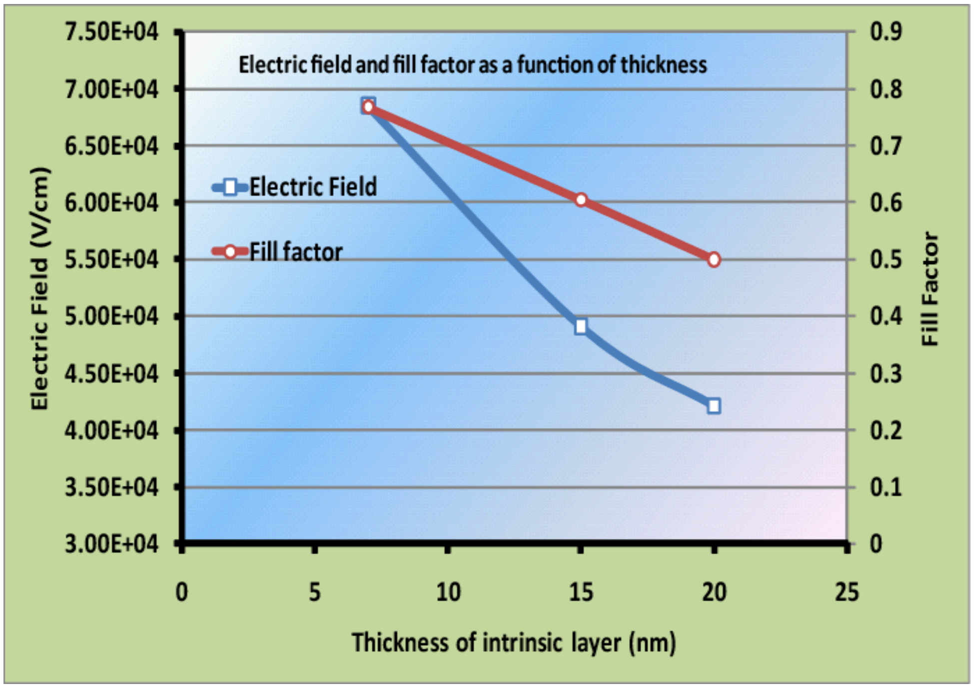

Figure 11. Electric field at heterointerface under thermal equilibrium and fill factor

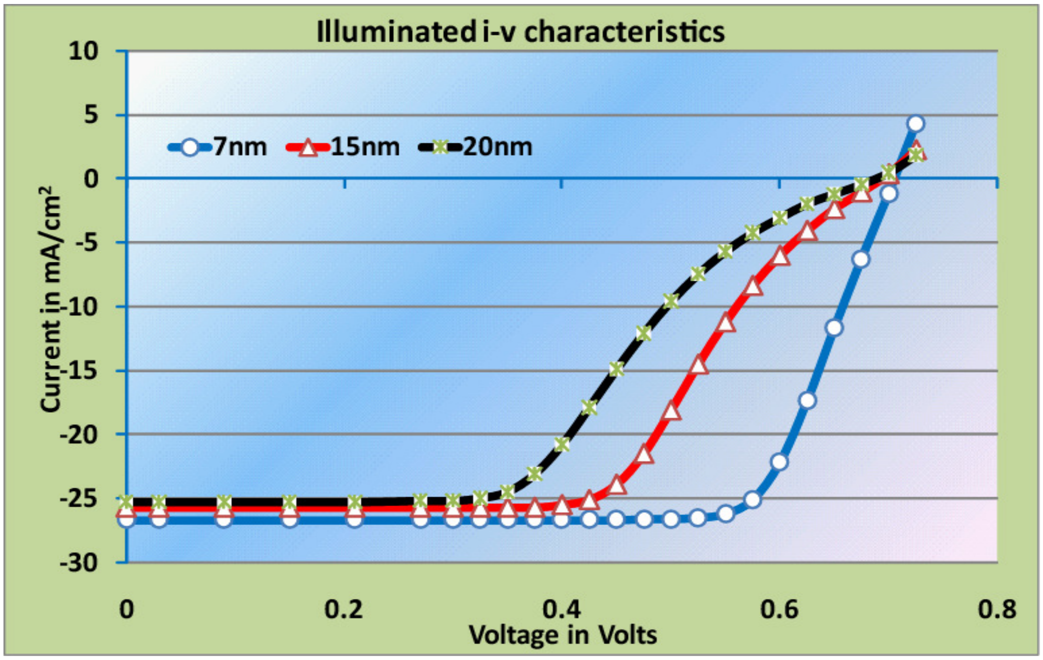

Figure 12. Simulated illuminated current-voltage relationship

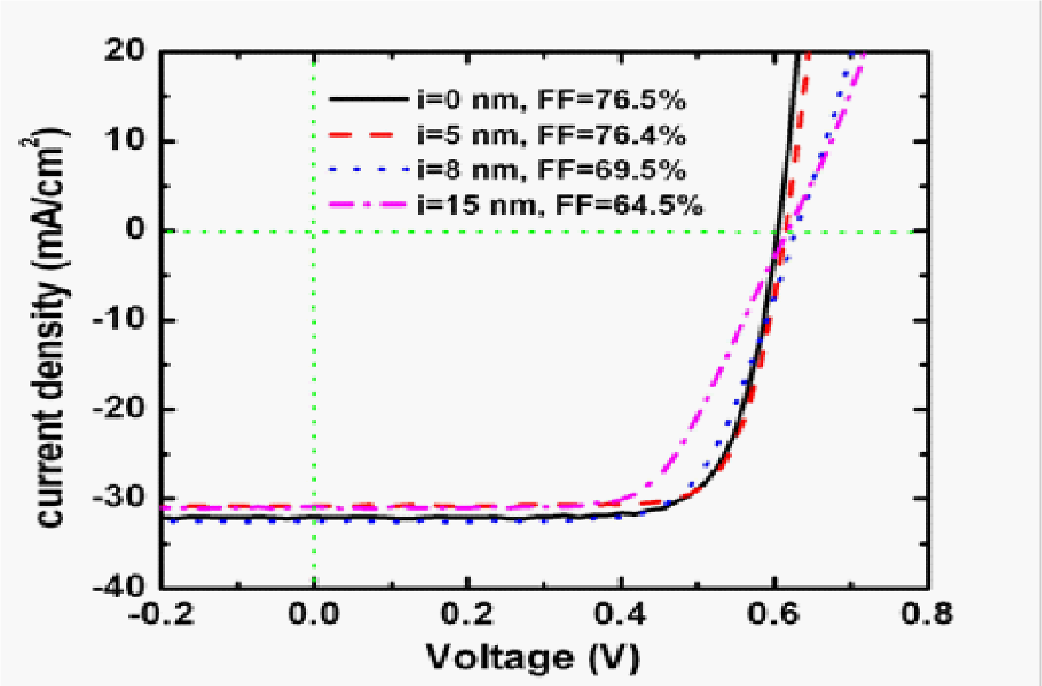

Figure 13. Experimental current-voltage relationship (obtained from reference 6)

The results show that the fill factor of a-Si/c-Si heterojunction solar cells decrease with increasing intrinsic layer thickness, the corresponding electric field at c-Si under thermal equilibrium decrease. The results can be explained as follows: In a-Si/c-Si heterojunction solar cell without the intrinsic layer an inversion layer is present at the heterointerface. Equation above shows that as the thickness of intrinsic layer increases, band bending decrease, resulting in devices with weakly inverted or no inversion at all for the c-Si surface. In devices, with a thin intrinsic layer as seen from the band diagram under thermal equilibrium in Figure 6, an inversion region is present near the heterointerface. The inversion region is followed by a depletion region and a quasi-neutral region. When the device corresponding to the band diagram in Figure 6 is put under forward bias, the voltage drop across the c-Si is primarily accounted for by the change in the width of depletion region and with negligible change in inversion region. This means that the electric field in the inversion region and the band alignment at the heterointerface is independent of the operating voltage and hence the series resistance encountered by the carriers in traversing through the inversion region and the intrinsic layer is constant. In devices with weakly inverted or no inversion at all for the c-Si surface under thermal equilibrium, the band bending at the heterointerface is affected by the operating voltage. When the devices are put into forward bias, the band bending has to decrease to account for the change in voltage. The average energy the minority carriers gain from the electric field is lower, resulting in a decreased rate of transmission through the intrinsic layer as explained in Chapter 4. This reflected both as voltage dependence and a higher value of series resistance for a-Si/c-Si heterojunction devices.

The experiments performed on the series resistance of intrinsic layer showed also temperature dependence for thicker intrinsic layer[46]. In the experiment reported in the reference, four different intrinsic layer thicknesses were chosen, denoted by 'half', 'normal', 'double' and 'triple'. The series resistance for device with 'double' intrinsic layer thickness showed a considerable temperature dependence while the effect was much muted for devices with intrinsic layer thicknesses of 'normal' and 'half'. The results seem to contradict that the dominant transport mechanism through the intrinsic layer is tunneling and also from the dependence of series resistance on intrinsic layer thickness, it seems to suggest that the thermionic emission cannot be the dominant mechanism. The apparent anomaly can be explained as follows: The third term in above equation for these experimental samples can be neglected. The band bending from above equation depends on the net sum of the first two terms and the first term decreases with lowering of temperature. In devices with thin intrinsic layer, the net sum still remains high in the temperature range the experiment are performed. But when the intrinsic layer is made thicker, this is no longer the case and a lowering of temperature decreases the band bending at the heterointerface. As discussed in chapter 4 and also mentioned in the preceding paragraph, this is accompanied by the lowering of the rate of transmission through the intrinsic layer and an increased series resistance. The effect is most pronounced for devices with intrinsic layer thickness of 'double'.

Equation above shows that similar results are expected when the level of doping in the emitter is decreased or when the defect density at the heterointerface increases and experimental results showing the effect of variation of these two parameters can be found in literature[6,47] . Hence an optimized a-Si/c-Si heterojunction solar cell has an inversion region at the heterointerface. As a consequence of the presence of inversion region, the series resistance is constant throughout the operating voltages of the solar cells. But in heterojunction devices without a strongly inverted surface, the series resistance is voltage dependent and higher resulting in devices with low fill factor. This however is not true when the band offset is too large to support the current and devices with low fill factor can result even for those with strongly inverted c-Si surface under thermal equilibrium. The implication of this condition on the performance of a-Si/c-Si heterojunction solar cell will be discussed in detail in the next section

5.5 Effect of band offset in the performance of heterojunction device

The effect of band offset at the heterointerface in the performance of a-Si/c-Si heterojunction solar cell is studied by varying the band gap of intrinsic layer. The valence band offset (VBO) and conduction band offset (CBO) are 0.45 eV and 0.15 eV respectively for the heterointerface with intrinsic layer band gap of 1.72 eV. While varying the band gap it is assumed that the variation of the band gap does not affect the ratio of 3:1 between VBO and CBO and the band gap difference between intrinsic a-Si and c-Si layer is split in this ratio. The band gaps considered for simulation are 1.8 eV, 1.72eV, 1.6 eV for intrinsic layer and the p-doped layer also has the same band gap. The results in Figure 15 show that with increasing band gap the fill factor drops. The result can be explained as follows: The increase in band gap results in lowering of transmission rate through the intrinsic layer. The holes reaching the heterointerface accumulate there and hence weakening the inversion of the bands present at the heterointerface. This results in further lowering of the transmission rate. Thus a poor device performance is obtained with increasing band gap of intrinsic layer. The experimental verification of the effect is obtained from ref. 6 and given below. In Figure 14, the black line corresponds to higher band gap while the red corresponds to lower band gap. The blue corresponds to the sample with the band gap as the red one but with a thinner intrinsic layer thickness (5 nm compared to 8 nm).

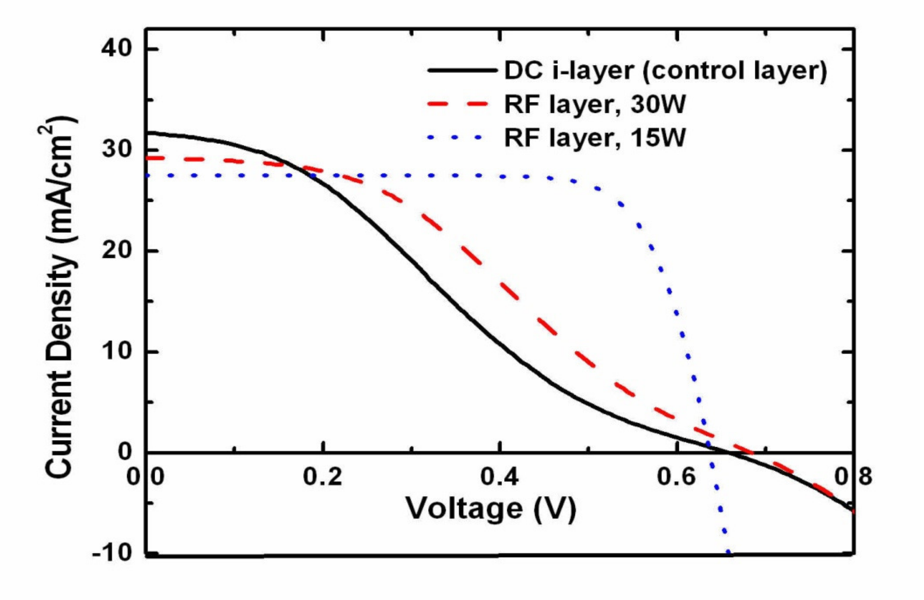

Figure 14. Experimental I-V relationship with different band gap of intrinsic layer (obtained from ref.6)

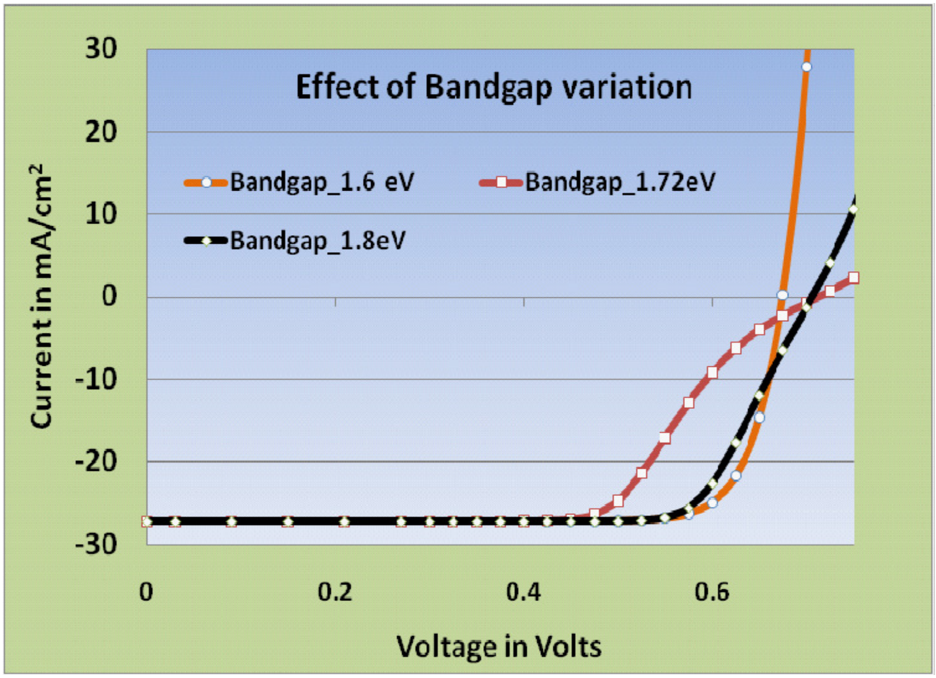

Figure 15. Simulated I-V relationship at different band gap of intrinsic layer

5.6 Conclusion

The performance of a-Si/c-Si heterojunction solar cell depends on the strength of electric field present at the c-Si surface. A high performance device requires a strong electric field implying the presence of a strongly inverted c-Si surface. The electric field and hence the inversion of c-Si depends on the doping of doped a-Si layer, the intrinsic layer thickness and the defect density at the heterointerface between a-Si and c-Si. The observations of the chapter and the previous ones will be used for outlining a novel theory described in the next chapter.

Chapter 6

NOVEL DEVICE THEORY OF OPERATION OF AMORPHOUS SILICON/ CRYSTALLINE SILICON HETEROJUNCTION SOLAR CELL

6.1 Introduction

Chapter 4 outlined the effect of band bending in the transport of minority carriers while Chapter 5 described the parameters affecting the device performance. In this chapter, the information will be put together in form of a novel theory that describes the operation of a-Si/c-Si heterojunction solar cell. The role of the constituent layers will be redefined in the context of the theory. A novel device concept utilizing the approach of selectively extracting carriers at the respective contacts is also proposed.

6.2 Novel device theory

In this section, a novel device theory explaining the operation of a-Si/c-Si heterojunction solar cell is outlined. The main premise of the theory is that an inversion region is present at the heterointerface and it affects the device performance. The inversion region is followed by the depletion region and the quasi-neutral region. The active junction is formed in c-Si. A high performance a-Si/c-Si heterojunction requires a strongly inverted region near the heterointerface throughout the operating domain of the device. Although the presence of an inversion region is a necessary condition, it is not a sufficient condition. The band offset also needs to be optimized depending on the intensity of illumination. A high enough band offset will cause an accumulation of charge at the heterointerface, thereby negatively affecting the inversion. In view of the novel theory, the role of the constituent a-Si layers on the top can be redefined. The doped a-Si layer on the top has a dual purpose: i) the layer acts to form the contact to the device and also induces a junction in c-Si. The top intrinsic layer in addition to providing surface passivation can also influence the transport of minority carriers, if not properly optimized. In the next section, a new class of device called ‘Selective Carrier Contact’ is proposed.

6.3 Selective carrier contact device

The dominant silicon solar cell technology is based on a diffused, top-contacted p-n junction on a relatively thick silicon wafer for both commercial and laboratory solar cells. The V_{oc} and hence the efficiency of a diffused p-n junction solar cell is limited by the emitter recombination current and a value of 720 mV is considered to be the upper limit. The value is more than 100 mV smaller than the thermodynamic limit of V_{oc} as applicable for silicon based solar cells[2]. Also, in diffused junction the use of thin wafers (< 50 um) are problematic because of the requirement of high temperature processing steps. But a number of roadmaps have identified solar manufactured on thinner silicon wafers to achieve lower cost and higher efficiency[3]. The selective carrier contact device provides a novel alternative to diffused p-n junction solar cells by eliminating the need for complementary doping to form the emitter and hence it allows the solar cells to achieve a V_{oc} of greater than 720 mV. Also, the complete device structure can be fabricated with low temperature thin film deposition or organic coating on silicon substrates and thus wafers can be utilized.

A schematic diagram of a selective carrier contact device is shown below in Figure 16. The diagram shows a crystalline silicon (taken to be n-doped for the discussion) with membrane layers, ‘layer-a’ and ‘layer-b’ on each side. The membrane layers have a band gap higher than the c-Si. The extraction of carriers from the device takes place through the contacts, ‘hole contact’ and ‘electron contact’ made to the membrane layer. Because of the band alignment, the surface of the c-Si in contact with ‘layer-a’ is strongly inverted and the active junction is formed inside the c-Si. In this discussion, irrespective of the position of carriers in the device (either in inversion region or quasi-neutral region), the majority and minority carriers will be electrons and holes respectively. Under illumination, the c-Si is the light absorbing medium and the photogenerated holes are collected on reaching the inversion region, which acts as the emitter of the solar cell. Due to the presence of the inversion region near the front interface, the concentration of majority carriers is strongly suppressed. The region acts as minority carrier filter, attracting the holes and reflecting back the electrons and thus provides excellent field induced front surface passivation. The band gap of ‘layer-a’ should be high so that the carrier concentration in ‘layer-a’ is negligible but either the thickness or band offset controlling the minority carrier transport is low enough to not impede the flow of minority carriers. Under these conditions, the ‘hole contact’ will almost exclusively extract or supply minority carriers. The band gap of the membrane layer, ‘layer-b’ on the rear has a similar requirement to ‘layer-a’ in that the band-gap should be high enough to have negligible carrier concentration in the layer. The distinction between the two layers is in the case of band-offset with c-

Si. The band offset for 'layer-b' should be such that the interface with c-Si acts as the mirror for minority carriers, reflecting the minority carriers into the bulk of c-Si while providing no impedance to the transport of majority carriers and under these conditions only the majority carriers are extracted or supplied from 'electron contact'.

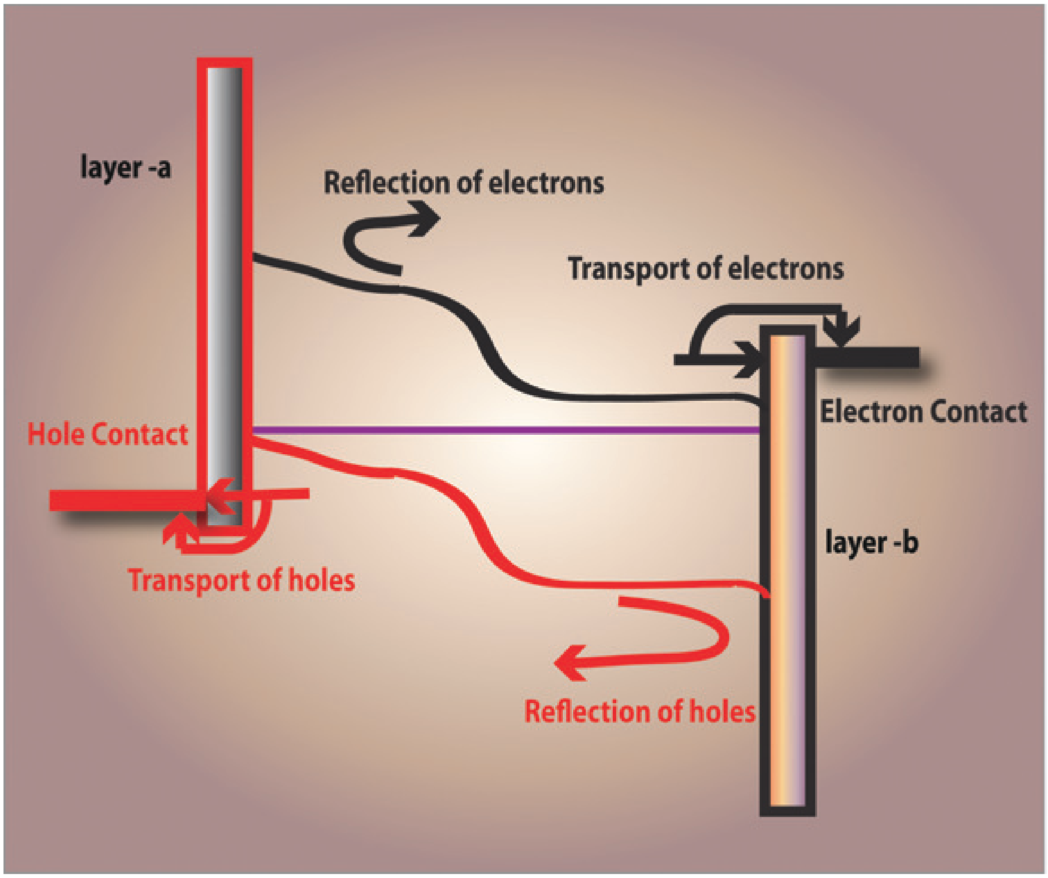

Figure 16. Schematic diagram of a selective carrier contact device. n-doped c-Si is the absorbing medium. The currents are extracted through contacts, 'Hole Contact' and 'Electron Contact'

The one-dimensional simulator PC1D is used to calculate the limiting V_{oc} as a function of device thickness at a fixed short-circuit current (42.5 mA/cm^2). The value of C_a is 1.66 x 10^{-30}. Both front and rear surfaces of c-Si in contact with 'layer-a' and 'layer-b' respectively are considered to be perfectly passivated and a

SRV value of zero, actually it is $1x10^{-5}$ cm/s to avoid numerical instability is taken for the simulation. At the front interface of n-doped c-Si, the band alignments mismatch of c-Si with the top layers causes a strong band bending resulting in an accumulation of holes and a strongly inverted region near the interface. The presence of the top layers can be modeled by putting a negative charge on the front surface of c-Si (positive for p-doped c-Si). The negative charge causes a positive image charge in the c-Si resulting in the band bending and an inversion region. In this work, since the surfaces are considered to be perfectly passivated, putting a charge on the rear surface is considered superfluous and no such attempt is made in the paper. The negative charge (Q) applied on the front surface defines the degree of inversion occurring in c-Si and hence the value of J_o. By varying from – 1x 10^{12}/cm^2 to -5x10^{12}/cm^2, no change in J_o is observed. Thus the surface is strongly inverted over this entire range of charge and a value of Q= -1x10^{12}/cm^2 is taken for the simulation. The bulk doping was varied from 1x10^{12}/cm^3 to 1x10^{15}/cm^3 to verify whether the change of the value has any effect on the V_{oc}. The variation caused negligible or no change in V_{oc} and the value of 1x10^{15}/cm^3 is taken for the bulk doping. The value of τ in this work is 10 ms^2. The simulation results show that on increasing τ by orders of magnitude (defect free bulk silicon) from the value of 10 ms, caused the V_{oc} to increase by a negligible amount of 2-3 mV. The V_{oc} values plotted as a function of device thickness is shown in Figure 17. The plots show that V_{oc} increases with decreasing device thickness, with an achievable V_{oc} of greater than 800 mV at 10 um. The devices thus provide a mechanism to bridge the gap between thermodynamic limits of V_{oc} and that achieved by diffused p-n junction solar cell.

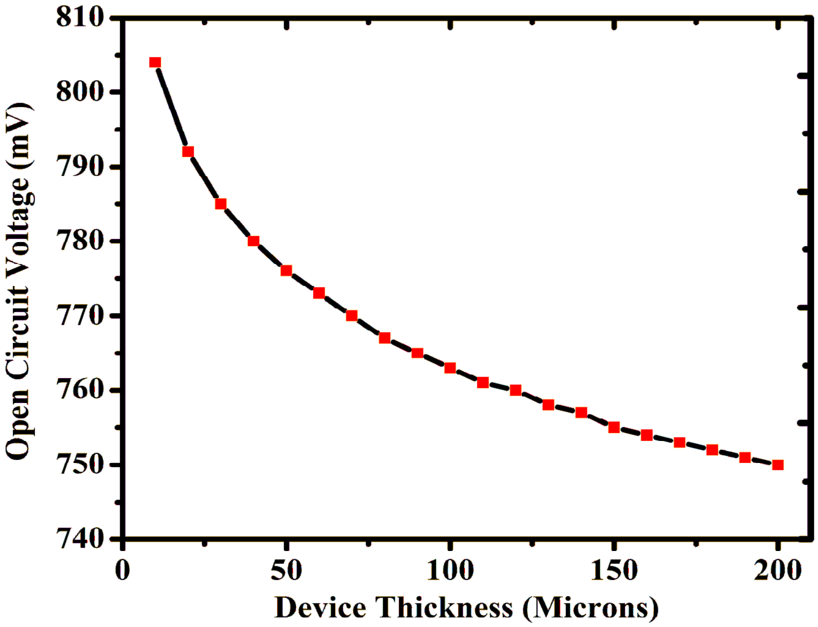

Figure 17. Limiting open circuit voltage as a function of thickness. The plot shows that with selective carrier contact device it is possible to achieve V_{oc} close to the thermodynamic limit

The simplest approach to obtain a selective carrier contact device is by depositing thin films of dielectric material with surface passivation quality on c-Si and with front/rear contact. One of the promising candidates is amorphous silicon (a-Si) or an alloy of a-Si (a-SiC or a-SiGe). The alloys provide a greater flexibility to tailor the band offsets, increasing the band bending and allowing current transport at all bias levels. The compound semiconductors of III-V (e.g. Gallium Phosphide) as the membrane layers can also be explored[48]. A further simplification in terms of processing and lower cost alternative is the application of organic materials on c-Si to fabricate the selective contact device. The organic layer has the dual role of reducing the defect density at the silicon surface while also causing strong band bending under the organic layer which induces a p-n junction on the front and acts as a mirror to the minority carrier on the rear. To realize the structure, the organic layer must first provide surface passivation, be chemically robust and offer the possibility of further functionalization such as chemically adhering to the encapsulant or another photovoltaic device. A wide range of well established attachment chemistry is available for a variety of functionalized organic molecules on silicon surfaces[49,50,51] and the systematic exploration of the effects of different attachment chemistry and molecular structure on device performance will be necessary to identify the ideal candidate for realizing the selective carrier contact device. A novel and revolutionary structure with both contacts on the rear to realize a selective carrier contact device is shown in Figure 18.In the structure a silicon with light trapping nanostructured layer on the front and a surface passivation layer on the rear is bonded to an encapsulant with charged films that form the induced junction and the metal lines that acts as contacts and current conducting element of the device. The structure incorporates a light trapping layer, allowing the usage of ultra-thin silicon and also the complete device can be fabricated without any substantial processing steps. Thus, allowing a dramatic reduction in cost and simultaneously obtaining high efficiency solar cells.

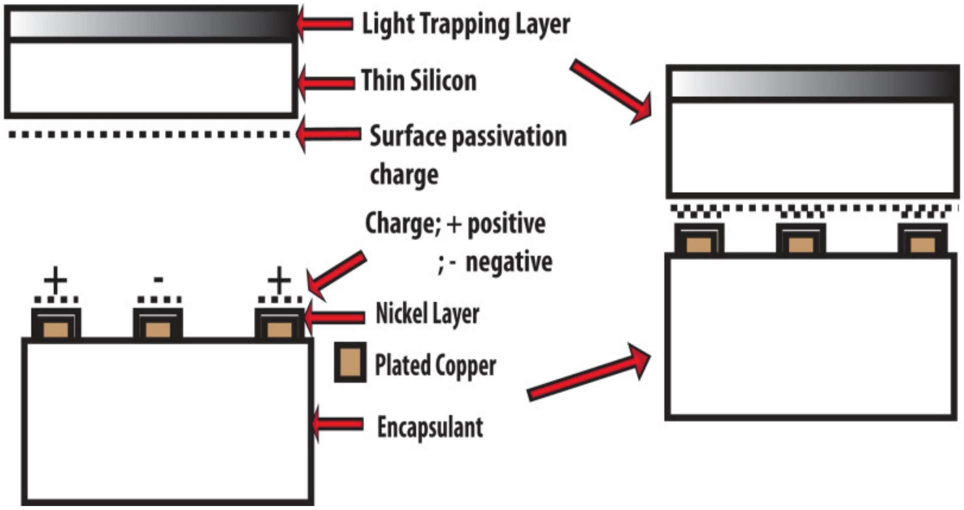

Figure 18. Novel device structure to implement selective carrier contact device. Both contacts are on the rear. The complete device can be fabricated without any significant processing step

6.4 Conclusion

In this chapter, a novel theory describing the operation of a-Si/c-Si heterojunction solar cell is outlined. The main premise of the theory is that an inversion region is present at the heterointerface in a-Si/c-SI heterojunction solar cell and the strength of the inversion region affects the device performance. The chapter also defined the role of the constituent a-Si layers. In contrary to conventional understanding, the doped a-Si and intrinsic a-Si layers have a role in the transport of minority carriers. Also, a novel device structure called ‘Selective carrier contact’ is proposed in the chapter and theoretical calculations are performed to understand the limiting open circuit voltage of the device. In the next chapter, a methodology to determine the recombination parameters of a-Si/c-Si heterojunction solar cell is described.

Chapter 7

DETERMINATION OF RECOMBINATION PARAMETERS OF AMORPHOUS SILICON /CRYSTALLINE SILICON SOLAR CELL FROM LIFETIME SPECTROSCOPY

7.1 Introduction

An accurate determination of the recombination parameters is essential to design and develop high efficiency a-Si/c-Si heterojunction solar cell. The letter describes a methodology to determine the recombination parameters through the measurement of inverse lifetime as a function of minority carrier concentration by Sinton lifetime tester and fitting the results with a polynomial of second order. The recombination parameter of a-Si/c-Si heterojunction solar cell that has attracted considerable attention is the effective surface recombination velocity (S_{eff}) at the interface between a-Si and c-Si (heterointerface)[28,47,52] Although S_{eff} is a good indicator to understand the surface recombination properties of the heterointerface, S_{eff} in addition to the surface recombination velocity depends on the band bending condition of c-Si at the heterointerface. The value of surface recombination velocity on the other hand is directly related to defect density at the heterointerface and hence is more useful in optimizing the heterointerface in terms of the defects arising from surface preparation and a-Si deposition. The intrinsic recombination parameters (auger and band-band) determine the limiting efficiency of high performance solar cell[53]. In this chapter, the surface recombination velocity (provided the bulk lifetime is known), auger and radiative recombination coefficient will be determined independently.

7.2 Theory

A schematic band diagram of a-Si (n)/c-Si (p) heterojunction with an intrinsic layer is shown in Figure 19. The band diagram is sketched from the top to an initial portion of the quasi-neutral region in c-Si. The n-doped a-Si induces a negative charge in the c-Si causing band bending and the amount of charge induced under thermal equilibrium depends on the properties of n^+ doped a-Si, the heterointerface and the intrinsic a-Si layer[54]. On the rear also, an intrinsic layer and a doped a-Si layer are present. The layers will induce a charge in c-Si but the effect is much less pronounced due to the same doping type of the substrate and the a-Si layer. In this work, for theoretical calculations the rear is taken to be perfectly passivated while for experimental results, no distinction will be made between front and rear surface and both of them is taken to behave identically to the minority carrier injection level. Under illumination, due to the band offset at the heterointerface, the photogenerated minority carriers (electrons in this case) accumulate at the heterointerface giving rise to a negative charge (Q_{het})[55]. The correlation of Q_{het} with excess minority carrier concentration requires rigorous modeling of transport mechanisms across the ordered/disordered heterointerface and Q_{het} is comparable to the induced charge only in poorly performing a-Si/c-Si heterojunction devices [55]. Under the assumption that Q_{het} is negligible to the total induced charge, the charge Q_S (opposite in polarity to the induced charge) due to the a-Si layers, the band bending ψ_s (positive in the direction shown in Figure 20), the surface electron (n_s) and hole (p_s) concentration and the minority carrier concentration (Δn) in the quasi-neutral region are related[56].

The inverse lifetime is related to carrier concentration as[57],

$$1/\tau = A+Bn+Cn^2$$

where, n is the carrier concentration. The coefficient A is the contribution of bulk and surface SRH recombination and is given by ,

$$A=1/\tau_{SRH} + 2S_{eff}/W$$

where, τ_{SRH} is the bulk SRH lifetime, S_{eff} is the effective surface recombination velocity and both front and rear surfaces are assumed to be equally passivated. W is the thickness of the device. Both τ_{SRH} and S_{eff} are carrier injection level dependent. $B=B_t+B_r$[58] where B_r and B_t are the radiative and trap-assisted auger recombinations respectively. C is the band-band auger recombination coefficient.

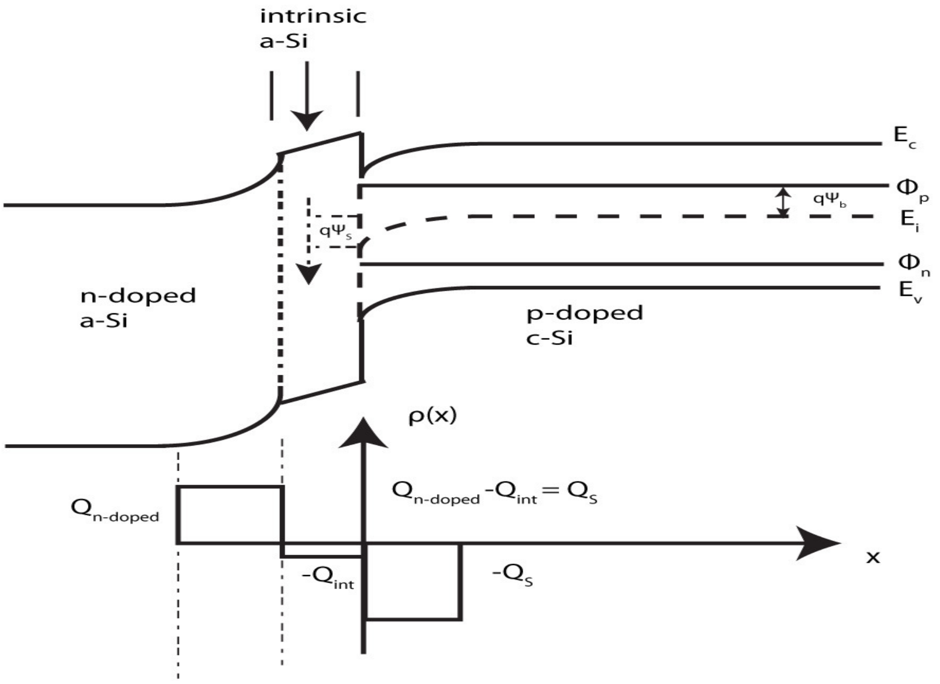

Figure 19. Schematic band diagram of a-Si/c-Si heterojunction solar cell. The space charge distribution in the device is also sketched

7.3 Simulation results

The one-dimensional device simulator PC1D is used to determine τ_{tot} as a function of Δn. The simulation is performed with p-doped c-Si of thickness 675 micron, doping of $1 \times 10^{15}/cm^3$ and a bulk lifetime (τ_b) of 5000 micro-second. The effect of a-Si layers are approximated by a positive charge (Q_s) and the desired ψ_s is obtained by varying the value of Q_s. The front surface recombination velocity (S_f) is 40 cm/s while the rear surface is perfectly passivated (S_r=1×10^{-5} cm/s, to avoid numerical instability). The radiative recombination coefficient (B) is 1.8 x 10^{-1559}. In Figure 20, a family of 3 curves (inverse lifetime curves) with each plotting Δn (horizontal axis, in cm^{-3}) as a function of $1/\tau$ (vertical axis, in s^{-1}) without the inclusion of auger and radiative mechanism are shown in Figure 20. The inverse lifetime curves are marked; str_inv (strongly inverted surface), weak_inv (weakly inverted surface), depletion (surface under depletion,). The curves correspond to different band bending conditions of the c-Si surface under thermal equilibrium. The curve for surface under depletion with the radiative recombination turned on (depletion_withRad) is also shown in Figure 20. The curves show that at low level injection, $1/\tau$ increases as the band bending condition changes from a strongly inverted surface to a surface that is under depletion. A surface under depletion has an equivalent concentration of electrons and holes and the recombination activity is much more enhanced than for a surface under inversion, where one type of carrier concentration is actively suppressed. At high level injection (HLI) as seen from Figure 20, the curves start to merge. In the set of simulations performed auger recombination has not been considered. The values as obtained for the intercept and slope agree with the values used in the simulation.

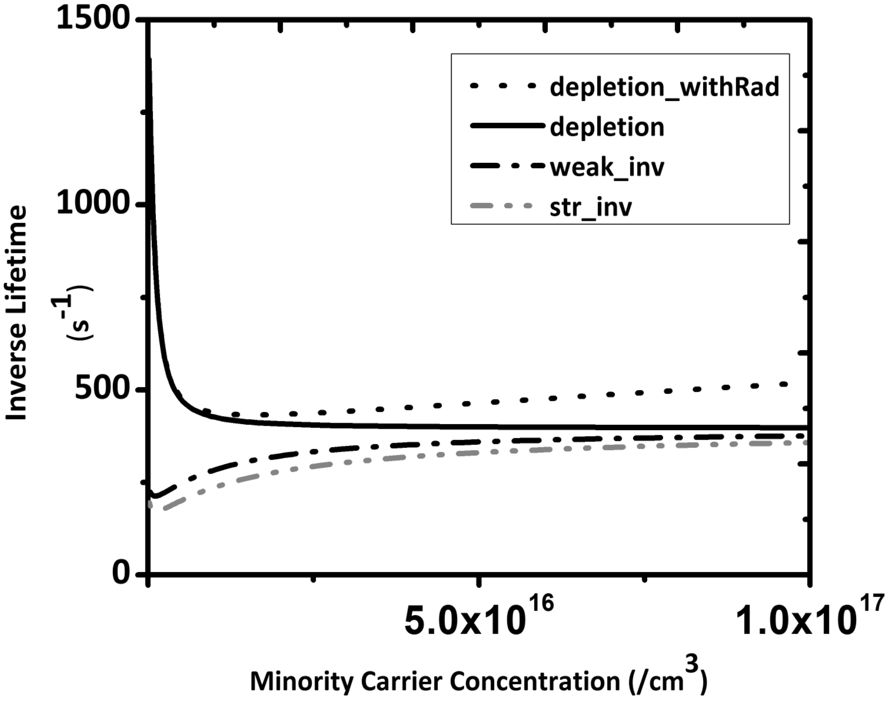

Figure 20. Inverse Lifetime curves at different band conditions with both auger and radiative recombination excluded.

7.4 Experimental results

Two sets of devices are considered for the work. Set 1 is fabricated on a 150 um n-doped c-Si substrates with as-cut surfaces while Set 2 uses 675 um p-doped substrates with single sided polished surface. The bulk lifetimes for both samples are in the order of miliseconds. In Set 1, the emitter layer thickness is 5 nm, the intrinsic layer and the doped layer on the rear are 7 nm and 5 nm in thickness respectively. The corresponding thicknesses for Set 2 are 100 nm, 7 nm and 10 nm. The emitter is p$^+$ doped a-Si in Set 1 while it is n$^+$ doped in Set 2. The thickness of the intrinsic a-Si on the top (buffer layer) is varied. The thicknesses are 7 nm, 10 nm, 20 nm and 30 nm for Set 1 while in Set 2, 30 nm sample is replaced by one with 15 nm thick buffer layer. The lifetime curves are obtained with Sinton Lifetime tester and are shown in Figure 21 and Figure 22

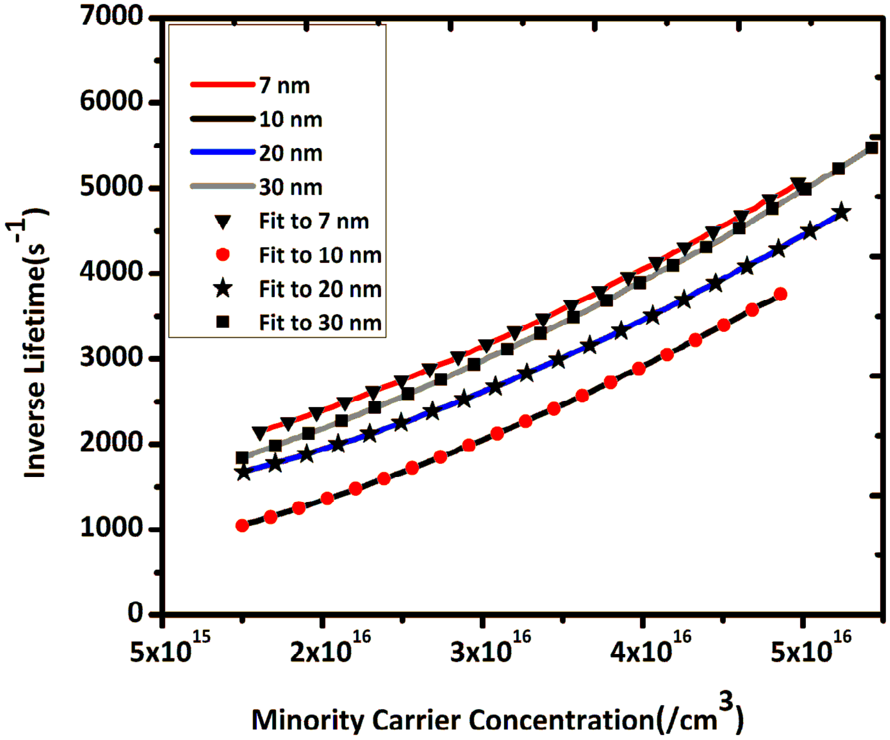

Figure 21. $1/\tau_{tot}$ as a function of Δn for Set 1 without auger correction. Set 1 is fabricated on a 150 um n-doped substrate.

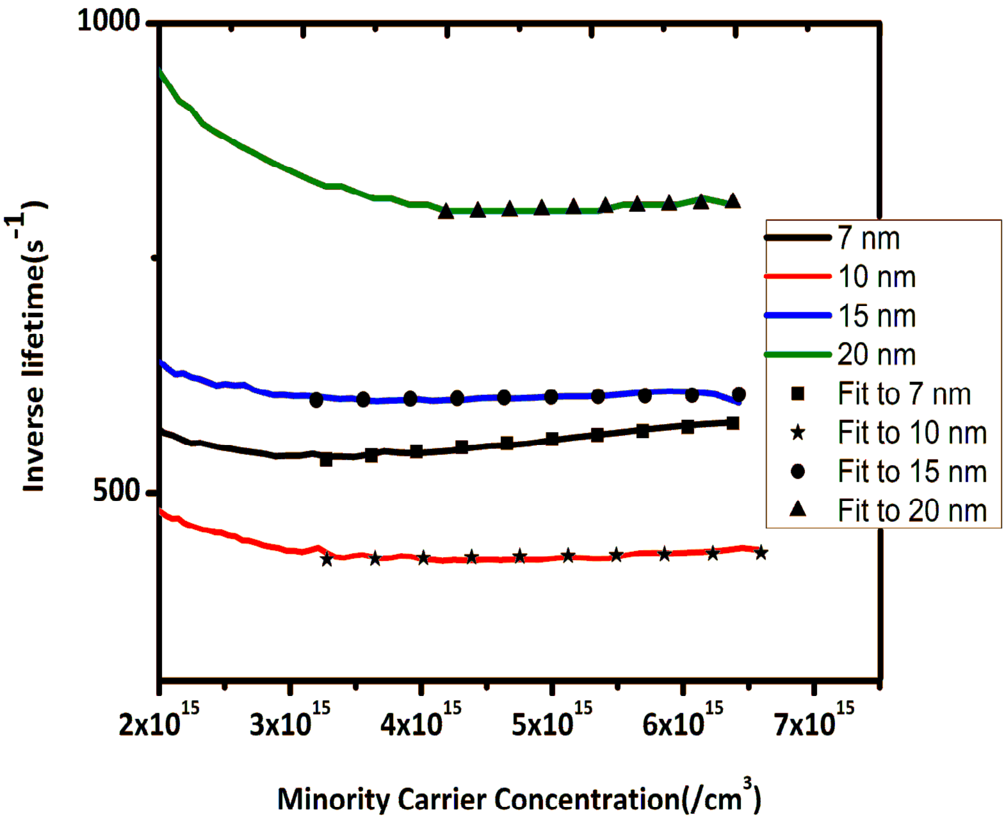

Figure 22. Auger corrected inverse lifetime as a function of Δn for Set B. The Set B is fabricated on 675 um p-doped c-Si substrate.

The experimentally obtained inverse lifetime curves (Figure 21) for sample Set 1 is fitted with equation above. The fitted data is shown by markers in Figure 21.The range of Δn over which the experiments are performed for Sample Set 2 is not high enough to determine auger coefficient independently as auger recombination is negligible compared to other recombination mechanisms. A value of C= 1.66 x10^{-30} is used to subtract the quadratic term corresponding to auger recombination. The auger corrected inverse lifetime is fitted with a linear function (A+Bx) to determine the intercept and the slope over the range of Δn as indicated by the markers. The markers show the fit of the function to the lifetime curves. The auger coefficients determined for Set 1 samples are in the high 10^{-31}. The values are close to 1.66 x 10^{-30} that is considered for auger coefficient at high level injection. The radiative recombination coefficients determined for the samples are in the order of 10^{-14}-10^{-15}, with the n-doped substrates having higher values than the samples with p-doped substrates. Although there is no consensus on the exact value of radiative recombination coefficient in silicon, the value is reported to be in the range of 10^{-14}-10^{-15}[60]. The recombination parameter corresponding to the bulk and surface recombination and given by the coefficient, A of the fitting is tabulated in Table 1. Considering that the bulk lifetime is same for the samples within a particular set, the values show that the samples with 7 nm buffer layer for both sets 1 and 2 have a poorer surface passivation than with 10 nm. This is expected as when the buffer layer becomes thinner, the defect rich doped layer on the top starts to interact with the heterointerface through recombination mechanism and thereby decreasing the surface passivation quality of the buffer layer. Also, it is observed that the surface passivation of samples with thicknesses higher than 10 nm has a poorer surface passivation. The effect may be related to the deposition time but no effort will be made in this letter to understand and explain the phenomena.

Table 1.

Value of coefficient A.

	7 nm	10 nm	15 nm	20 nm	30 nm
Set 1	1548	557	N/A	1243	1252
Set 2	494	422	592	785	N/A

Conclusion

The chpter describes a methodology to determine the recombination parameters of a-Si/c-Si heterojunction solar cell from lifetime spectroscopy. Under HLI, the c-Si surface at the heterointerface is under flat-band condition and a fit of the lifetime curve with an equation of appropriate order will determine the recombination parameters. The auger and radiative recombination coefficient determined by the technique agrees well with the previously reported values. The bulk and surface recombination parameters correspond to a well passivated surface with high bulk lifetime. The technique in spite of being effective and efficient in determining the recombination parameters has some shortcomings. The methodology to determine the three recombination parameters independently can only be performed with a value of minority carrier concentration in excess of 1x 10^{16}/cm^3 and with silicon surface under flat-band condition over the entire range of Δn used for the fitting. Hence the technique cannot be used for samples with low bulk lifetime or poorly passivated surface. Another shortcoming is that the surface recombination velocity, S determined by the technique can be used to predict the performance of only the a-Si/c-Si heterojunction solar cell with an inversion region at the heterointerface.

Chapter 8

MATERIAL SELECTION FOR MULTIPLE QUASI FERMI LEVEL SYSTEM IN QUANTUM WELL

8.1 Introduction

A major disadvantage of a solar cell based on a conventional p-n junction is that the sub band-gap photons are not absorbed. A MQFL system based on nanostructured devices address the problem. A schematic diagram of a MQFL system is shown in Figure 23. As seen from the figure, in a MQFL system there is a spatial existence of three quasi-fermi levels (QFL). The QFL's marked μ_c and μ_v correspond to the QFL of the conduction band and valence band respectively while μ_I is for the confined carriers in the well. The simultaneous spatial existence of three QFLs allows the occurrence of three complementary radiative absorption-emission processes as shown in Figure 23. The transitions as marked 2 and 3 assist in the absorption of sub band gap photons while transition 1 is due to the absorption of above band gap photons. This results in an enhanced absorption of photons in a MQFL system when compared with a conventional p-n junction solar cell. Since, the contacts are made to the higher band gap material (barrier) there is no degradation of open circuit voltage and hence such a system is capable of achieving efficiency higher than the conventional p-n junction when used as a solar cell.

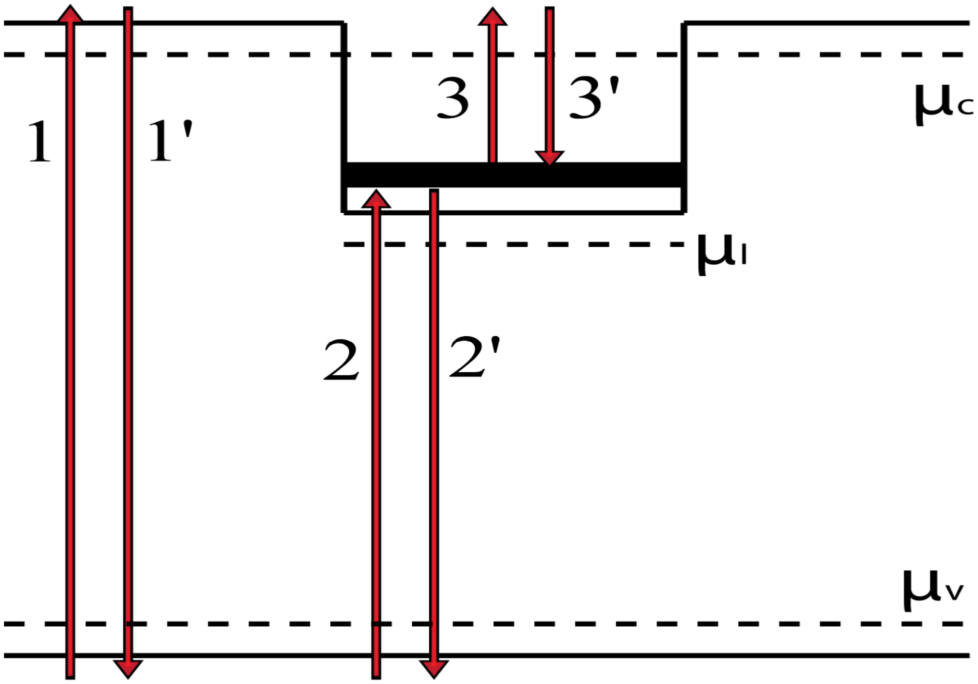

Figure 23. Schematic diagram of a MQFL system

The majority of previous works in this field have concentrated on QDs[61-63]. Preference has been given to QDs over QWs[64] because of the discrete energy level in QDs compared to continuous energy level in QWs resulting in an increased loss of carriers by phonon scattering, thereby decreasing the probability of having a radiative intraband transition. However, quantum well infrared photodetector[65] shows that the intraband transition from well to the continuum of states in the conduction band is possible for QWs with high escape rate from the well under reverse bias. Moreover, the collection efficiency in QW solar cells can be high in forward bias if the electrical field is maintained above a critical value[66]. Provided that carriers can be collected as indicated by such experimental results, QW devices have the advantage of increased absorption volume and more straight forward fabrication. Consequently, it is important to analyze the optimum material combination for QW based MQFL system.

8.2 Material selection criteria for QW based MQFL system

The choice of material combinations for a MQFL system using QW is dictated by two major criteria: one is that that material combinations should be lattice matched to each other as well as to commonly available substrates (GaAs, InP, Ge and Si) while the other is the bandgap requirements to optimize the performance of the structure as a solar cell. The criteria used for selection of the material combination are given below:

a) The lattice mismatch between the barrier and the commonly available substrate to be within ± 2 %
b) The lattice mismatch between the well and the barrier or the common substrates to be within ± 2 %

Detailed balance calculations have shown that the barrier band gap should be greater than 1.2 eV and the band offset (either in valence band or in conduction band, as applicable) should be greater than 0.4 eV[67] . The detailed balance calculations are performed assuming a negligible band offset, either in the conduction band or in valence band. In this work, the material combinations which give the band gap equal to or near the optimized value is given preference. Also, to be consistent with detailed balance criteria, the band offset either for valence band or conduction band has been taken to be negligible ($<3\ k_bT$).

8.3 Calculation of material parameters

The calculations to identify the material combinations are performed on 9 diads and 18 triads of Gallium, Aluminum, Indium, Antimony, Phosphorus and Arsenic with GaAs and InP as the substrate. The calculations also include the mentioned diads and triads as the material for the well with Si or Ge as the barrier and the corresponding substrate (Si as substrate if Si is the barrier). In case of III-V compounds, the combinations that give direct band gap are only considered.

The band parameters like band-gap, band offset, and elastic constants are obtained for III-V semiconductors are obtained from ref. 68 while for Silicon and Germanium it is obtained from ref.45. For an alloy of the III-V material, the band parameters are obtained by using Vegard's law and the non-linearity with the change in composition is accounted for by using a bowing parameter[69,70].

In quantum well, the layers are often grown pseudomorphically and the effect of strain in modifying the band gap has to be taken into account. The effect of strain in modifying the band structure at k=0 i.e. at the band edges has been included in the model by using 6 band **k·P** method[71]

8.6 Detailed Balance Calculations

The detailed balance calculation provides the maximum theoretical efficiency of a solar cell. The detailed balance calculations are based on the premise that each absorbing photons give rise to an electron and the total current is proportional to the difference between the rate of photon absorption and the radiative emission processes[72]. The rate of radiative emission is determined by the separation of the quasi-fermi levels.

In case of a three level transition system, the equation needs to be modified to take into account the third quasi-fermi level [73,74]. In the detailed balance calculation of a MQFL system, it is assumed that the net flux due to the complementary radiative absorption-emission processes,2-2´ and 3-3´ is zero. This means that the confined carriers in the well does not contribute to the current and the current is extracted from the higher band gap material (barrier) only. The current in MQFL system is proportional to the net flux corresponding to the complementary set of radiative transitions, 1-1´and 3-3´ while the corresponding voltage is the difference between μ_c and μ_v.

8.7 Results

The results of the calculations are tabulated in table 2. The columns 2, 3 and 4 correspond to the barrier material, well material and the substrate. In column 5, it is mentioned whether the confinement is in the valence band or in the conduction band. The columns 5 and 6 give the value of the confinement and the theoretical maximum efficiency under 1 sun concentration and blackbody radiation (Efficiency) respectively.

Table 2.

Material Combinations for MQFL system

Barrier	Well	Substrate	Confinement (in meV)	Efficiency (in percent)
$Al_{0.63}In_{0.37}As$	$InAs_{0.16}P_{0.84}$	InP	587	42.5
$Al_{0.33}Ga_{0.67}As$	Ge	Ge	1071	38.43
$Ga_{0.53}In_{0.47}P$	Ge	Ge	1214	43.9
$Al_{0.27}Ga_{0.73}As$	$GaAs_{0.83}Sb_{0.17}$	GaAs	1102	42.14
$Ga_{0.36}In_{0.64}P$	$GaAs_{0.75}Sb_{0.25}$	GaAs	670	39.05
$Al_{0.54}In_{0.46}As$	$GaAs_{0.33}Sb_{0.67}$	InP	793	26.55
$Ga_{0.28}In_{0.72}P$	$GaAs_{0.73}Sb_{0.27}$	InP	637	37.62

8.8 Conclusion

The work identifies the material combinations that can be used to realize a three level transition system based on quantum well device structure. The material search encompasses the 9 diads and 18 triads of III-V semiconductors with GaAs and InP as the substrate. It also includes the above diads and triads as the barrier and Ge or Si in the well with the corresponding substrate. Since, quantum wells are grown pseudomorphically, the effect of strain in modifying the band edges has been included by using 6 band **k.P** method. The maximum theoretical efficiency of the material combinations that satisfy the criteria for a three level transition system has been calculated by using detailed balance calculations. The calculations show that $Al_{0.63}In_{0.37}As$/ $InAs_{0.16}P_{0.84}$ and GaInP/Ge with InP and Ge as the substrate respectively are the two combinations giving the highest theoretical efficiencies. The efficiencies of the combinations are 42.5 % and 43.9 % compared to the theoretical maximum efficiency of 47 %. The material system of AlInAs/InAsP has been previously used and demonstrated in optoelectronic devices such as 1.3 um laser while GaInP/Ge is extensively used in triple junction solar cell.

Chapter 9

ABSORPTION COEFFICIENT FOR MULTIPLE-QUASI FERMI LEVEL SYSTEM IN QUANTUM WELL

9.1 Introduction

Chapter 9 calculates the absorption coefficients of a MQFL system. The calculations of absorption coefficients are necessary to determine the rate of radiative transitions. In this work, absorption coefficient of one of the transition (transition from valence band to confined state in the quantum well) for a MQFL system is derived from Fermi's golden rule while the other two absorption coefficients are calculated based on previously published work. The results are discussed with respect to AlInAs (barrier)/InAsP (well) quantum well system that is previously identified as one of the material combinations for a MQFL system.

9.2 Theory

A MQFL system as discussed in chapter 8 exhibits three sets of complementary radiative absorption-emission processes (two interbands and one intraband transition) due to the simultaneous spatial existence of three quasi-Fermi levels as shown in Figure 23. Quantum well (QW) based devices have been proposed as a candidate material for exhibiting three level transitions[74]. As seen from Figure 23, a MQFL system when used as a solar cell will allow for the absorption of sub band-gap photons with the current being extracted at a voltage determined by the higher band gap and hence providing a means to overcome the Shockley-Quissier efficiency limit [75] in a solar cell. The six transitions in Figure 23, involves three absorption coefficients. The absorption coefficient for transitions marked 1-1’ and 3-3’ are analogous to the absorption coefficient for band to band transition in bulk semiconductor and for the transition from confined states to the continuum in Quantum well infrared photodetector and is discussed in detail elsewhere[76],[59]. The transition 2 in Figure 23, involves a transition from a non-confined state in the valence band to the confined state in the conduction band and no reference exists in the literature about the calculation of this absorption coefficient. In this chapter, the absorption coefficient of the transition is derived from Fermi’s golden rule under a few simplifying assumptions about the absorbing medium. It is assumed in the calculation that ε-k dispersion relationship is parabolic[77]. The thickness of the well layer is so chosen that there is only a single energy level (ground level) in the well. The second energy level is either in the continuum or within 3 kT below the continuum energy level and in either case to be treated to be part of the continuum rather than the confinement. In the valence band the degeneracy at k=0 is removed by the effect of strain. Under tensile strain (compressive strain), the heavy hole band (light hole band) is above the other at k=0. In this calculation, only the band that corresponds to the lowest energy level at k=0 is considered and the presence of the other two bands (heavy hole or light hole, as applicable and spin-split off band) is neglected. The effective mass approximation is assumed to hold true and only direct band to band is considered. The principle of conservation of momentum in the transition, as applicable holds in the calculation.

The rate of transition from Fermi’s golden rule and the absorption coefficient for this transition is given below.

$$W_{i\to f} = \frac{2\pi}{h}|M|^2 g(h\omega)$$

$$\alpha(E_k)=\frac{1}{4\pi\varepsilon_0}(2\pi e^2 h)/2\mu m_o^2 c E_k\ |M|^2 g_k f(E_i)(1\text{-}f\ (E_j))$$

In above equations, E_k is the energy of transition, $|M|^2$ is the optical transition matrix element, g_k is the number of states available for transition, f (E_i) is the probability that the initial state is full while 1- f(E_j) is the probability that the final state is empty. The other terms are constant with their usual meaning.

The joint density of state is calculated based on the transition energy, E_k. The initial state of the optical transition, E_i is a non-confined state in the valence band while the final state of the transition, E_j is a confined state in the confinement of the conduction band. A transition involving quantum well requires that the in-plane momentum needs to be conserved[78]. Assuming a parabolic band and taking the zero of the energy to coincide with the maximum of the valence band, the energies E_i and E_j can be written as,

$$E_i=-\frac{h^2}{8\pi^2 m_v^*}k^2-\frac{h^2}{8\pi^2 m_v^*}k_z^2$$

$$E_j=\frac{h^2}{8\pi^2 m_c^*}\ k^2+E_{g1}+\Delta E_g$$

$$E_k=E_j-E_i=\frac{h^2}{8\pi^2}\left(\frac{1}{m_c^*}+\frac{1}{m_v^*}\right)k^2+\frac{h^2}{8\pi^2 m_v^*}k_z^2+E_{g1}+\Delta E_g$$

k_x and k_y are the in-plane momentum with, $k^2 = k_x^2 + k_y^2$, k_z is the out-of plane momentum, E_{g1} is the gap between the minima of the conduction band and the maxima of the valence band in the well. m_c^* and m_v^* are the effective masses of electrons and holes respectively. ΔE_g is the shift of the energy state due to the confinement and h is the Planck's constant.

Equations above show that the constant energy surface for transition energy, E_k is a rotational ellipsoidal with the length of the axes in x and y direction been given by, $1/m_c^*+1/m_v^*$ while the axis in the z-direction is given by $1/m_v^*$.This then gives the joint density of states, g_k.

$$g_k(E_k)=\frac{8\pi m^*}{h^3}\sqrt{2m_v}^{*}\sqrt{E_k-E_{g1}-\Delta E_g},$$

where, $1/m^*=1/m_c^*+1/m_v^*$.The optical transition matrix element, $|M|^2$ can be written as [78], $|M|^2 = |M_{cv}|^2O^2$, where, $|M_{cv}|^2$is the bulk transition matrix element and O^2 is the square of the wave overlap function. The optical transition under discussion has the final wave-function in the confined state of the conduction band and the initial wave-function in the valence band. In the calculation of the wave-functions, it is considered that the barrier is of finite height with a zero applied electric field. The barrier width is finite in dimension but much greater that the well width, so that the wave-functions from the adjacent wells do not interfere. The device structure hence can be just a single quantum well with barrier on both sides or a multiple quantum well structure with a periodic repetition of the single quantum well structure as shown in Figure 23.

9.3 Results

The results are discussed with the material combination of $Al_{0.63}In_{0.37}As$ as the barrier and $InAs_{0.16}P_{0.84}$ as the well. The thickness of the well considered in this work is 4 nm and only a single confined state is present in the well. The barrier is 30 nm on each side of the well and can be considered infinite so that the validity of the single quantum well holds. The absorption coefficient of transition

2 as discussed in reference 76 depends on the angle of incidence and a value of 45 degree to the direction of growth is taken in this work. Figure 24 shows the plot of absorption coefficient of transition 1 as a function of energy. The optical transition as seen from Figure 24 begins at energy of 1.8 eV, which is the band-gap of $Al_{0.63}In_{0.37}As$ with correction for strain.

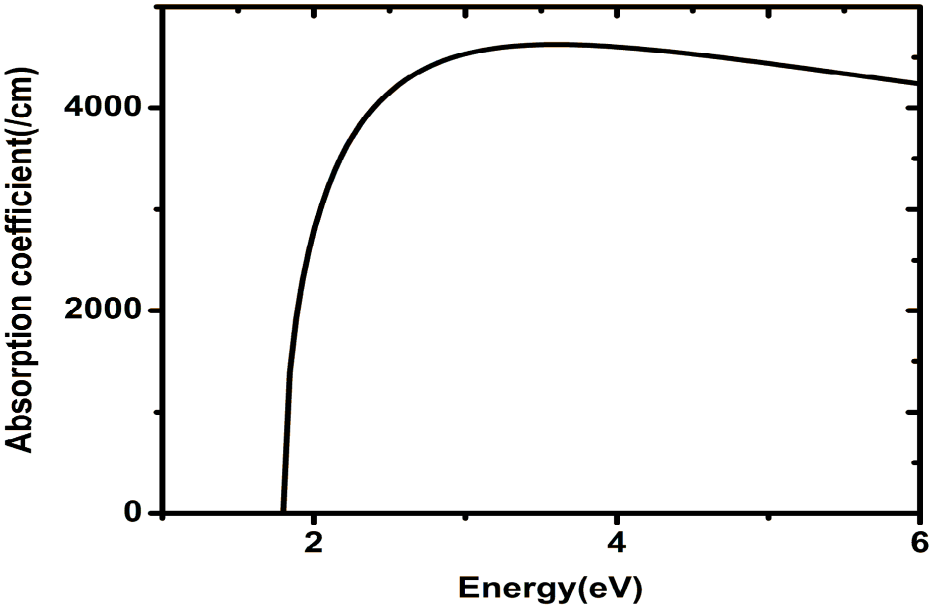

Figure 24. Absorption coefficient for Transition 1. The absorption coefficient has a value of zero below 1.8 eV, which is the band-gap of $Al_{0.63}In_{0.37}As$

The plots of the absorption coefficient for transitions 2 and 3 are shown in Figure 25 and Figure 26 respectively. The plots show that as the electron concentration in the well increases, absorption coefficient for transition 2 increases while that for transition 3 decreases. The physical explanation of the phenomena is that as the electron concentration increases, the number of carriers participating in the upward transition from the bound state of the quantum well to the continuum increases, thereby increasing the absorption coefficient. Simultaneously, the number of available states for upward transition from the valence band to the confined state in the well decreases and hence the absorption coefficient for transition 3 decreases.

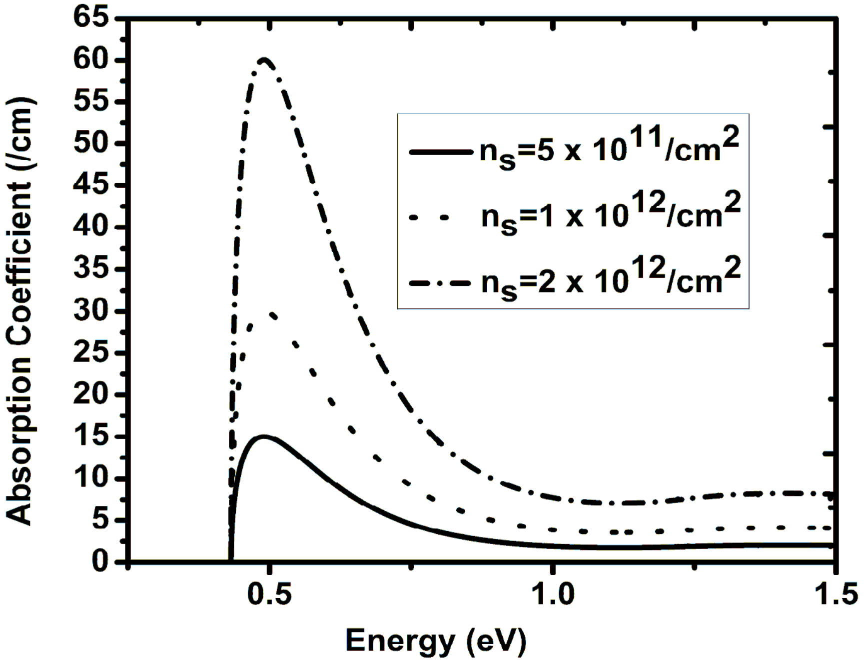

Figure 25. Absorption coefficient of transition 2. n_s is the sheet electron concentration in the well. The absorption coefficient increases with increasing n_s

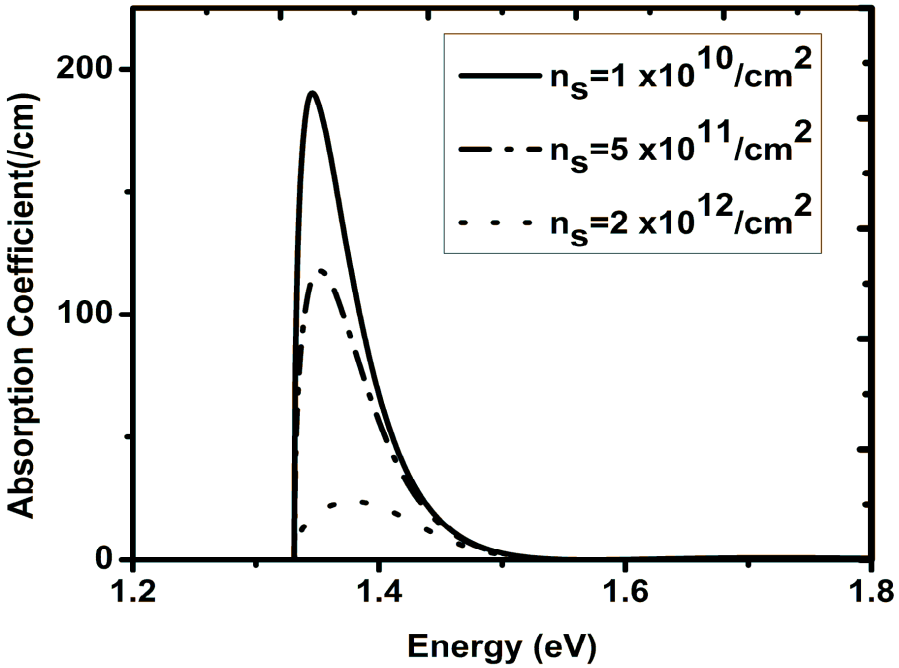

Figure 26. Absorption coefficient of transition 3. n_s is the sheet electron concentration in the well. The absorption coefficient decreases with increasing n_s

9.4 Conclusion

In this work, the absorption coefficients of $Al_{0.63}In_{0.37}As$/ $InAs_{0.16}P_{0.84}$ are calculated. The calculation shows the non-linearity arising due to the filling of available states in the quantum well. The absorption coefficient for the optical transition in the barrier is much higher than the absorption coefficient for transitions in the quantum well. The absorption coefficients for transitions 2 and 3 balance each other, which means that as the value of one of them increases the other decreases. Thus, if the scattering of carriers from the continuum of the well to the confinement is negligible, an electron population with its own quasi Fermi level can be maintained in the well and thus a MQFL system can be realized.

Chapter 10

INFLUENCE OF GROWTH CONDITIONS ON THE COMPOSITION OF PSEUDOMORPHIC GALLIUM ARSENIDES ANTIMONIDE

10.1 Introduction

The chapter discusses the growth of epitaxial layers of GaAsSb by molecular beam epitaxy on GaAs (001) substrates with the Sb/As flux ratio varied for growth temperatures of 470 C, 500 C and 530 C. The results are fitted using a non-equilibrium thermodynamic (NET) model where the GaAsSb ternary compound is treated as a homogenous mixture of GaAs and GaSb.:

10.4 Experimental Aspects

All of the samples in this study were grown in a Applied Epi GenIII MBE system on semi-insulating GaAs(001) substrates. The system contains both arsenic and antimony cracker cells to ensure dimer rich group V species for growth. The cracker zones were held at 950 C and 1000 C for the arsenic and antimony crackers respectively for all of the growths. The arsenic overpressure for all of the samples was varied between 1.7 - 5.0 x 10^{-6} torr as measured by a nude ion gauge beam flux monitor. For each sample the temperature was calibrated by finding the de-oxidation temperature by observing the RHEED pattern and adjusting the pyrometer reading to read 580 C. Each sample had a 100nm buffer layer of GaAs grown at 580 C before the growth rate of GaAs was checked, and adjusted if necessary, to be approximately 0.4 monolayers/s. Subsequent measurements of the grown layers confirmed that the growth rate for the GaAs was this value and that the growth rates for the GaAsSb layers were approximately 0.42 monolayers/s. A further 100nm of GaAs was then grown before the temperature was dropped to 470 C, 500 C or 530 C. After refreshing the surface with growth of approximately 5nm of GaAs, the Sb shutter was opened and a 30 s growth interrupt performed with the surface exposed to both Sb and As. A 5nm layer, for lower Sb compositions, or 10nm layer, for higher Sb compositions, of GaAsSb was grown followed by 5nm of GaAs. The temperature was then raised to 580 C and for the 10nm samples 70nm of GaAs was grown giving a total GaAs cap of 75nm. For the 5nm samples a further 15nm of GaAs was grown and the process repeated 5 times giving a periodic 5nm/25nm GaAsSb/GaAs structure. A final 50nm layer of GaAs was grown at 580 C to give a total cap thickness of 75nm.

The Sb compositions of the GaAsSb were analyzed using double axis crystal high resolution X-ray diffraction (HRXRD) carried out using a Philips X'Pert high resolution double axis diffractometer. The X-ray source consisted of a Cu Kα_1 emission tube emitting to a multi-layer focusing mirror collimator followed by a four bounce Ge (220) Bartels monochromator giving an incident wavelength of 1.54056 Å. A 3 bounce Ge (220) analyzer crystal focused the diffracted X-rays on to a proportional detector on the detector arm allowing the collection of triple crystal ω-2θ rocking curves and both symmetric and asymmetric reciprocal space mappings.

10.5 Results and Discussion

The sample structure used for studying the composition, namely a 5 quantum well structure or single 5 or 10 nm layer, allowed easy fitting of

HRXRD spectra for determining the composition. Shown in Figure 1 is the (004) ω-2θ rocking curve for a single layer sample with a growth temperature of 530 C and a Sb flux of 2.25 x 10^{-7} torr and As flux of 1.7 x 10^{-6} torr. The peak associated with the GaAsSb layer is fairly broad since it is 10nm thick and there are clear interference fringes suggesting a high quality interface and crystal quality. The FWHM of diffraction peaks for the substrate and epilayers were checked and compared to measured values for high quality GaAs epilayer samples and indicated pseudomorphic growth. Further to this, asymmetric RSMs were taken for the higher Sb content samples, with Figure 2 showing that obtained for a 5nm GaAsSb layer grown at 470 C with an Sb content of 31.5%, with the collected signal being the (224) diffraction for an incident (004) beam. As can be seen an exemplary mapping with no evidence of any significant relaxation of the grown layer was collected. If there was significant relaxation of the 5nm GaAsSb layer (above roughly 10^4 cm^{-2}) the signals from the substrate and grown layer would not be aligned along the Q_x axis. The perfect alignment of the signals indicates that the relaxation of the layer is below the detection limit and the growth is essentially pseudomorphic. Similar results were found for other high Sb contents confirming that all of the grown layers are pseudomorphic.

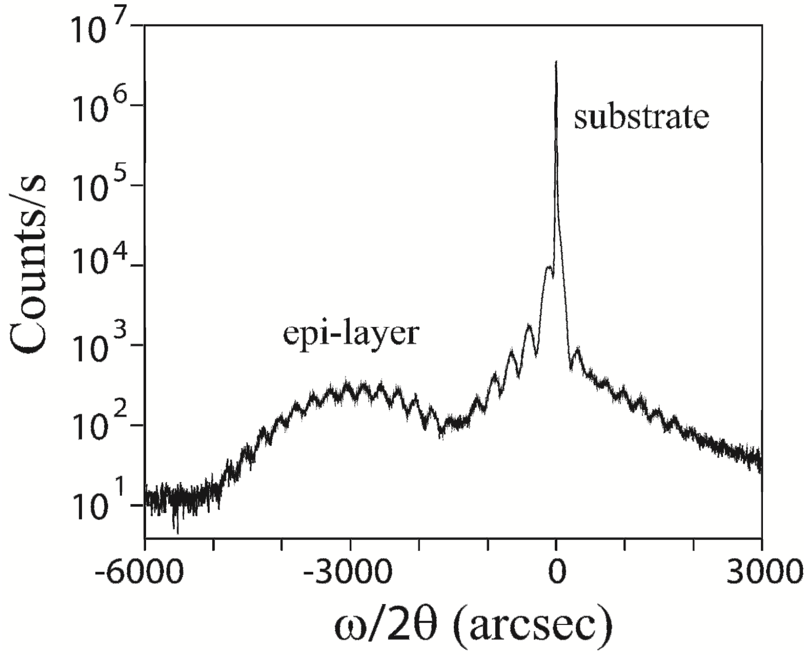

Figure 27. A typical ω-2θ rocking curve for single 10nm layer GaAsSb-GaAs sample in this case with growth temperature of 530 C and a Sb flux of 2.25 x 10^{-7} torr and As flux of 1.7 x 10^{-6} torr.

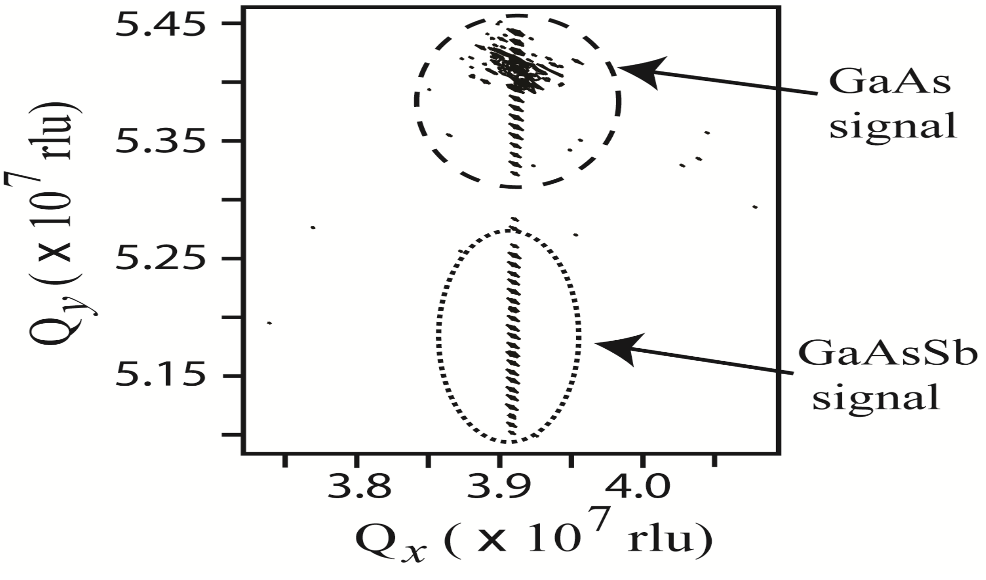

Figure 28. Asymmetric Reciprocal Space Mapping for a single 5nm layer sample with Sb composition ~ 31.5 %, taken around the (224) signal for a (004) incident beam.

The measured Sb content for all of the samples as a function of Sb/As flux ratio for the growth temperatures 470 C, 500 C and 530 C are plotted in Figure 29. An uncertainty in the composition of 2% absolute was estimated, as well as a 0.01 uncertainty in the flux ratio, to account for drift in the Sb and As fluxes during growth, these uncertainties are indicated by the error bars associated with each data point. There are two immediately identifiable features of these results; firstly an increase in growth temperature gives a lower Sb composition for a set Sb/As flux ratio, indicating that, whilst Sb is incorporated in preference to As in this growth temperature range, increased temperature sees this preference lessened. The second easily identifiable feature is that for 470 C and 500 C the Sb composition saturates, though this is not seen for the 530 C results. This type of effect has been previously observed and attributed to Sb-Sb competition for incorporation and the imperfect accommodation of different atom sizes and bond lengths in the alloy[79,80] . We attribute this saturation to lattice strain induced melting as proposed by Bottomley.

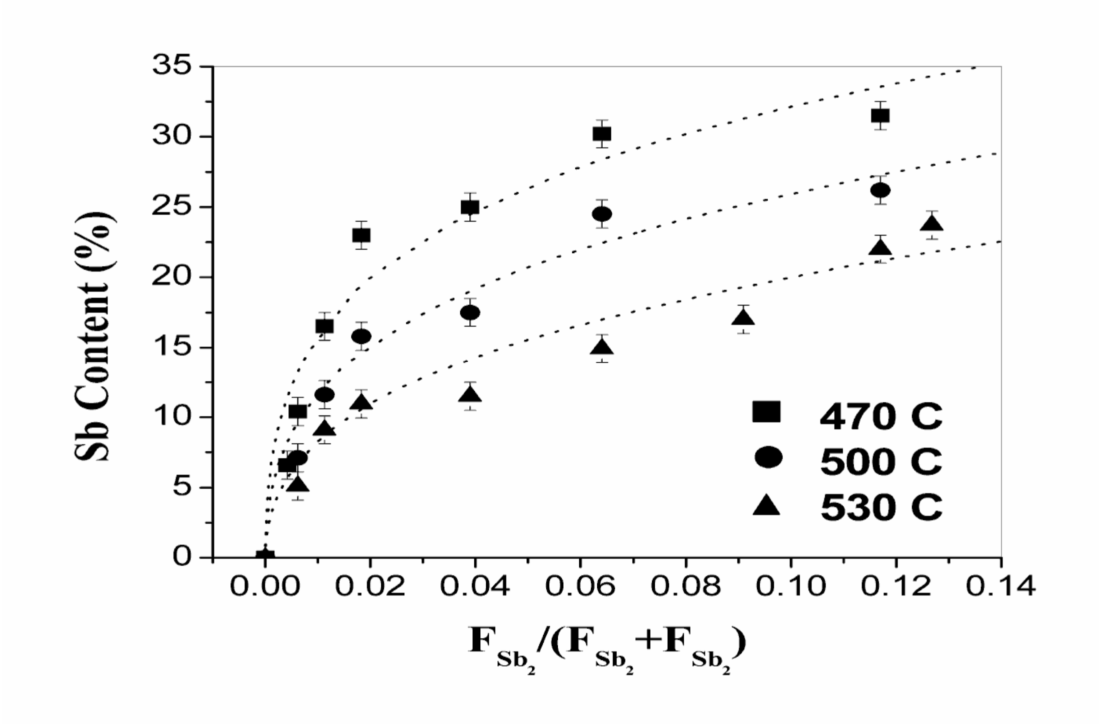

Figure 29. Measured Sb content for all of the samples as a function of Group V flux ratio for the growth temperatures 470 C, 500 C and 530 C

There are a few intriguing features that become apparent, firstly, the curvatures of each temperature set are not the same with the 470 C data showing a pronounced knee in comparison to the 500 C data and the 530 data. Secondly, the compositions are getting closer in value as the flux ratio is increased. In fact the implication is that the composition may be relatively pinned for intermediate flux ratios for all of the growth temperatures with only the rapidity with which the pinned composition range is reached being changed by the growth temperature.

This behavior can be understood by keeping in mind some factors already discussed. Firstly, the Sb-Sb and Sb-As competition for lattice sites and the accommodation of the different bond lengths helps to explain why the composition can become relatively pinned at intermediate flux ratios. Secondly, the rate of re-evaporation of the Group V elements changes for each growth temperature so that at higher temperatures it becomes increasingly likely that Sb will be re-evaporated before it can be incorporated into the lattice, explaining the lower sensitivity to increases in the measured flux ratio. This means that in order to fully explain these results it is necessary to calculate the ratio of available Sb_2 to available As_2 at the growth surface. This ratio would by necessity be dependent on both temperature and the current composition to account for all of the effects just discussed.

One final comment relates to the practical question of obtaining reproducible compositions. As was noted earlier the Sb content rises rapidly for low flux ratios before flattening out somewhat. This can be problematic when low Sb content is required when we consider the drift in flux for a Group V element during growth, making controllable and reproducible low composition growth difficult. These results suggest that as the temperature is increased the composition region of high flux ratio sensitivity is reduced and the range of flux ratio where the composition varies near linearly with flux ratio is increased. Reciprocal Space Mapping indicated that the higher growth temperature does not adversely affect the crystal quality suggesting that for the range of Sb composition up to roughly 20-25% a higher growth temperature may be preferred. Of course, when this is done the control of the composition profile at the GaAs-GaAsSb interface would need to be addressed as this has proven to be dependent on temperature and flux [81] as well as interrupt time.

10.6 Conclusions

Pseudomorphic GaAsSb layers have been grown by MBE on GaAs(001) substrates at various growth temperatures and antimony to arsenic flux ratios. When the results were analyzed by application of the non-equilibrium thermodynamic model the expected increase in the Sb/As equilibrium flux ratio with growth temperature was observed. It was found that the data could be best fit only when the interaction energy used was 1/10th of previously published values, indicative of epitaxial effects overcome the miscibility gap predicted for GaAsSb. Also, the difference between each temperature set of data decreases with increased flux ratio with all three temperature sets inferred to be approaching a common range of compositions where pinning is seen. Finally, the results show that as the temperature is increased the range, both in composition and flux ratio, where the composition increases relatively linearly and gradually with flux ratio is expanded with the onset of this region at lower composition values. It is suggested that this behavior with higher growth temperatures may be used to give greater control over the composition for low Sb content GaAsSb layers on GaAs.

Chapter 11

INFLUENCE OF SOAK TIMES ON PROPERTIES OF GALLIUM ARSENIDE ANTIMONY/GALLIUM ARSENIDES INTERFACES

11.1 Introduction

Chapter 11 looks at the effect of exposing the Gallium Arsenide (GaAs) growth surface to an antimony (Sb) and arsenic (As) flux immediately prior to growth of GaAsSb. Three samples that were nominally identical except for the length of the Sb/As flux soak were grown and analyzed by XRD and photoluminescence (PL). The XRD results presented suggest that exposing the GaAs surface to the Sb/As flux for 30s may improve the GaAs-GaAsSb interface roughness compared to a sample with no Sb/As soak, but that this advantage is lost for an Sb/As soak of 60s, implying an optimum Group V soak time. A band diagram calculated using the model solid theory and a four band **k.p** model was calculated and the GaAs-GaAsSb interfaces modified according to the HRXRD results. Fitting of PL spectra taken at 80 K with emission spectra based on the inferred band diagram shows good agreement, implying the proposed band diagram is correct. Some of the implications of these results in terms of GaAsSb growth on GaAs are briefly discussed for different growth temperatures and fluxes.

11.2 Experimental Details

Three nominally identical GaAsSb/GaAs multiple quantum well (MQW) samples were grown on semi-insulating GaAs(100) substrates in an AppliedEpi GenIII molecular beam epitaxy system. The As_2 species was supplied by a valved cracker source with a bulk temperature of 420 C and cracker zone temperature of 950 C. The Sb_2 species was supplied by an all pBN valved cracker source[82] with the bulk temperature set to 550 C and the cracker zone temperature at 1000 C. The Beam Equivalent Pressures for the As_2 and Sb_2, measured using a nude ion gauge, were 5×10^{-6} torr and 9.8×10^{-8} torr, respectively. Gallium was supplied by a standard Knudsen type thermal source with the temperature at 994 C giving GaAs and GaAsSb growth rates of 0.4 and 0.42 monolayers/s, respectively, for each sample. The temperature of the substrate was calibrated by observing the transition of the Reflective High Energy Electron Diffraction pattern from diffuse to streaky and adjusting the pyrometer settings to make this temperature 580 C. A 200 nm GaAs buffer was grown at 580 C and after checking the GaAs growth rate another 100 nm of GaAs was grown, also at 580 C. The temperature was then decreased to 500 C and the MQW structure grown. After growth of a thin layer (~5 nm) of GaAs there was a growth interruption where the Sb and As shutters were both open for an allotted time. For the samples designated as A, B and C, the soak times were 0 s, 30 s and 60 s, respectively. The Gallium shutter was then opened to grow 5 nm of GaAsSb and then the Sb shutter was closed and a further 5 nm of GaAs was grown. The temperature was raised back to 580 C and a further 15 nm of GaAs grown before the process was repeated another 4 times to obtain the MQW structure desired. A 75 nm GaAs cap completed the samples.

The compositions of the samples were determined using double crystal x-ray diffraction to obtain ω-2θ rocking curves about the (004) reflection of GaAs. A Philips X'Pert high resolution double axis diffractometer was used with the X-ray source consisting of a Cu Kα_1 emission tube emitting to a multi-layer focusing mirror collimator followed by a four bounce Ge (220) Bartels monochromator, giving an incident wavelength of 1.54056 Å. A 3 bounce Ge (220) analyzer crystal focused the diffracted X-rays on to a proportional detector on the detector arm allowing the collection of triple crystal ω-2θ rocking curves and reciprocal space mappings. Fitting of the rocking curves gave Sb compositions for samples A, B and C of 15.3 %, 15.8 % and 16.5 % respectively with an uncertainty estimated to be 1 % absolute. Reciprocal space maps (RSMs) were then obtained for each sample in a triple crystal x-ray diffraction arrangement in the [110] and [1-10] directions. Further to these measurements photoluminescence (PL) was used to characterize the samples. The samples were loaded into a liquid nitrogen cooled cryostat and the PL spectra were obtained under excitation from a continuous-wave laser with output wavelength of 532 nm and power 27 mW. The luminescence from the PL samples was collected using an iHR320 Horiba Jobin Yvon spectrometer equipped with a TE-cooled InGaAs array.

11.3 Results and Discussion

After the composition of the samples had been determined by ω-2θ rocking curves in a double crystal arrangement the samples were also aligned for a triple crystal arrangement and reciprocal space mappings were performed. Initially, wide scans in both ω and ω/2θ directions were performed. A second finer scan was then performed in order to collect data concentrated around the first five satellite peaks due to the MQW structure of the samples. Each data point had a 5 second collection time and the ω range was ±0.1 degrees about the central maximum. Two Reciprocal Space Maps (RSMs) were obtained for each sample, one in the [110] direction, and one in the [1-10] direction. The [110] direction was obtained by initially using the major flat of the whole wafer for visual alignment and then searching for the angular position giving the maximum counts. After the [110] RSM was complete the wafer was rotated 90° and a fine alignment procedure was performed to remove any misalignment or tilt in the sample.

The RSMs for samples A, B and C in the [110] direction are given in Figure 28. As can be seen the amount of diffuse scattering around each satellite peak (labeled with peak order) is minimal suggesting that the GaAsSb/GaAs interface is relatively sharp. The large amount of diffuse scattering around the GaAs peak for each sample, labeled in each map, also suggests that there is generation of defects that are propagated through to the substrate. The low counts of this diffuse scattering and the lack of any evidence of relaxation in asymmetric RSMs indicate that, for all of the samples studied, the total thickness of GaAsSb is below the critical value. This is consistent with previous experience of growth of $GaAs_{0.88}Sb_{0.12}$ on GaAs, under similar growth conditions, where a critical thickness of just above 30 nm was inferred. It would be expected that growth of samples with larger total thicknesses of GaAsSb would see the defect density increase until coalescing to form dislocations in the crystal structure to accommodate the lattice mismatch between the GaAs and GaAsSb.

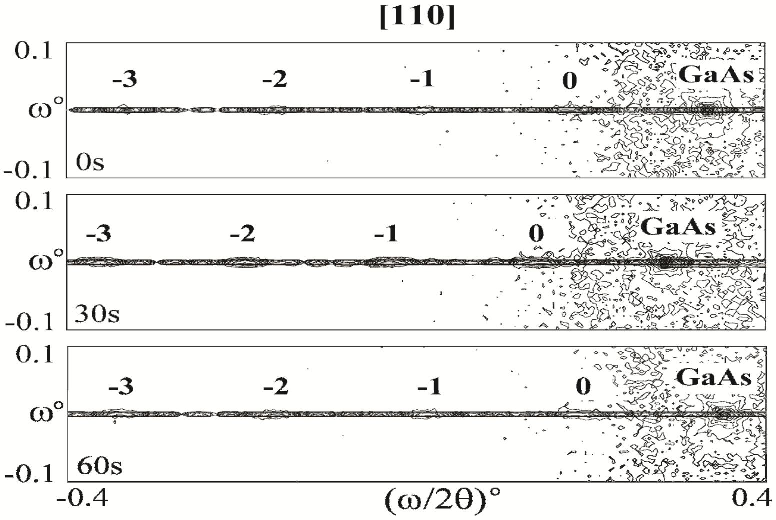

Figure 30. Reciprocal space maps for samples A, B and C taken in the [110] direction, with the Sb/As soak time noted for each mapping.

The RSMs for A, B and C taken in the [1-10] direction are shown in Figure 29. Like the maps taken in the [110] direction there is a great deal of low count diffuse scattering around the GaAs peak, again indicated by an arrow. This further confirms that the samples studied have a total GaAsSb thickness close to, but below, the critical value. In marked contrast to the maps taken in the [110] direction these maps show significant low count diffuse scattering about the MQW satellite peaks with the patterns showing an elongation parallel to the ω axis. This elongation in ω when the RSM is taken in one direction and the lack of any such elongation (indeed there is little to no diffuse scattering) when taken in the perpendicular [110] direction suggests that there is a corrugated interface between GaAsSb and GaAs [83] with the long axis of the corrugation in the [110] direction. The low counts of the diffuse scattering also suggest the corrugation is very shallow, most probably only 1-2 monolayers, a result consistent with previous reported results[84]. It is impossible to say if there is any periodic nature to the corrugation without using a high intensity X-ray source such as a synchrotron to provide greater counts and determine if there are any indicative features in the diffuse scattering about the satellite peaks. Most significantly it can be seen that the level of diffuse scattering around each satellite peak as well as the amount of elongation in ω is minimized for a Sb/As soak time of 30 s.

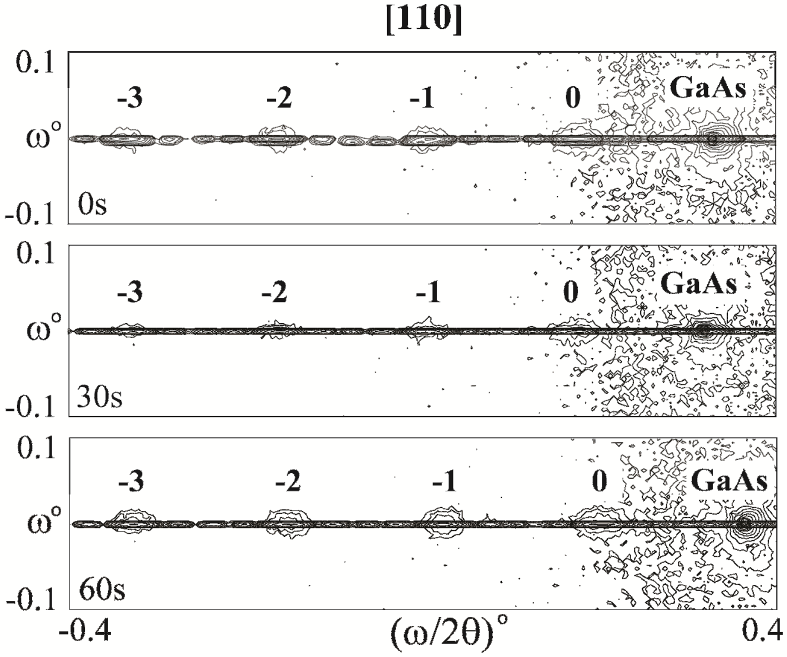

Figure 31. Reciprocal space maps for samples A, B and C taken in the [1-10] direction, with the Sb/As soak time noted for each mapping.

Shown in Figure 30 is how the interface between the GaAs and GaAsSb is deduced to evolve with the soak time looking towards the (110) plane. As can be seen, for the 30 s case the interface is relatively continuous with a fully two dimensional layer of GaAsSb meaning an atomically sharp interface between the layers. By contrast, for the 0 s and 60 s cases, the exchange between Sb and As means an uneven interface with GaAsSb penetrating not as a continuous sheet but with sections of GaAsSb a monolayer deeper than the other sections. It is this feature which leads to the diffuse scattering about the satellite peaks in the [1-10] RSMs for the 0 s and 60 s cases. The exchange spiking is not evenly distributed throughout the interface but occurs in such a way that the spikes are elongated in the [110] direction preferentially. In terms of Figure 3, the interface looking towards the (110) plane would be similar but with the penetrating GaAsSb being wider than in the (110) case. It would seem, based on our results, that the formation of the GaAsSb-GaAs interface formed by Sb-As exchange when under the Sb/As overpressure proceeds in such a way that monolayer thick GaAsSb strips are formed and that as the soak time increases these strips expand in the [1-10] direction, until at some optimum soak time, a complete 2 dimensional layer is formed. If the soak time continues beyond this optimum time the process repeats.

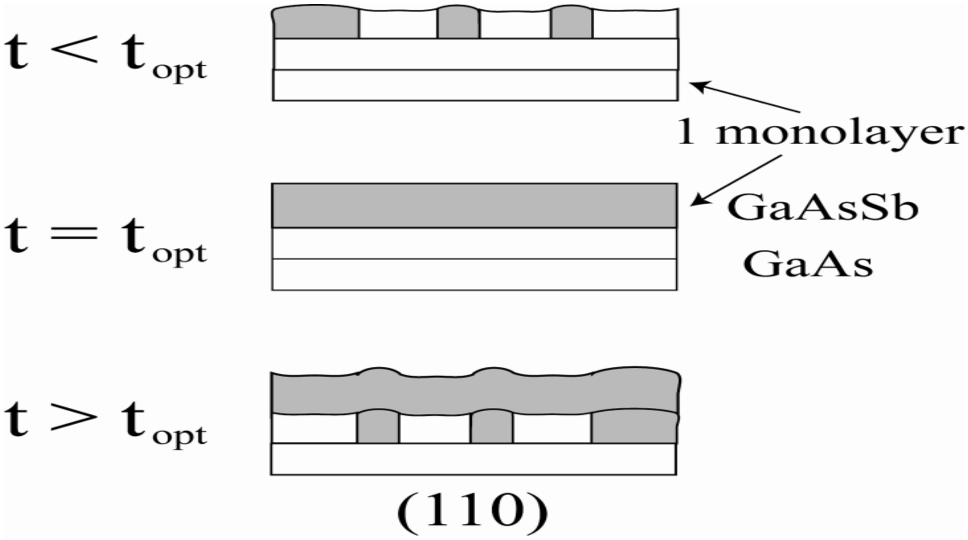

Figure 32. Proposed evolution of the GaAs-GaAsSb interface as the soak time is increased, showing the monolayer ‘spiking’ due to Sb/As exchange. The ‘spikes’ are elongated in the [110] direction.

The XRD results show the structural effect on the GaAsSb-GaAs but don’t give any information about the effect of the interfaces on the properties of the grown layers. To investigate this, photoluminescence (PL) measurements were performed on all of the samples. In order to properly interpret the results of the PL measurements the band structure expected for the samples was calculated. This was done using a model solid theory with the effects of strain included[85] and finding the hole confined energy levels using a four band **k.p** model [86] (no confined electron energy levels were found using a single particle Schrodinger equation with a strain modified potential and effective mass for GaAs). The structural parameters used in the calculations were all taken from Vurgaftman et al. [68]. A schematic of the calculated band edges for a $GaAs_{0.84}Sb_{0.16}$/GaAs quantum well at 80 K is shown in Figure 31 with a type II heterostructure predicted, in which the holes are confined, with different confinement energies for light and heavy holes. Also indicated are the calculated confined energy levels for the holes, the predicted conduction band offset of 0.057 eV and the GaAs thickness of 25 nm meaning no confinement of electrons is to be expected. The calculated transition energies between the GaAs conduction band edge and the first two confined energy levels for heavy holes as well as the first confined energy level for light holes are indicated.

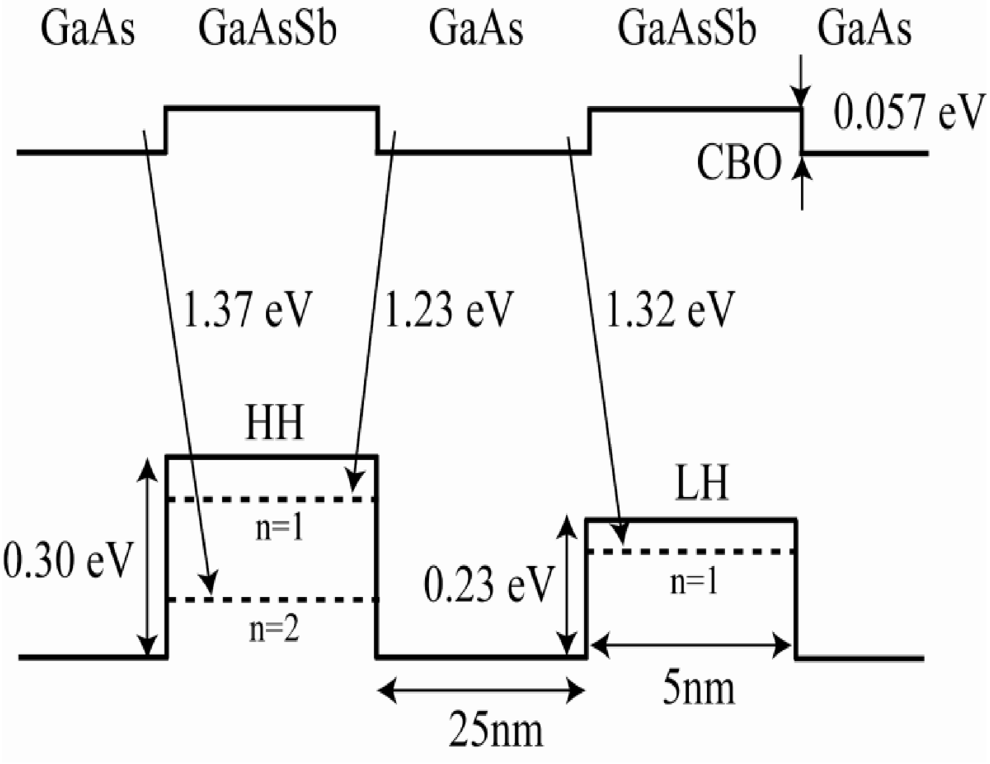

Figure 33. Schematic of the derived band diagram for a $GaAs_{0.84}Sb_{0.16}$/GaAs multiple quantum well sample at a temperature of 80 K, showing the type II band alignment for the Sb contents considered.

PL spectra obtained at 80 K for all three samples are displayed in Figure 32 with the PL signal plotted logarithmically. This allows a shoulder feature in the lower energy portion of the spectra to be seen for each sample, a feature ascribed to defects due Sb segregation at the GaAsSb/GaAs interface [87], as it is centered at an energy below the lowest predicted energy transitions, namely the ground state heavy hole transition. Further investigation of this peak, by say, excitation power dependent PL, would be necessary to make any conclusions regarding the relative densities of the Sb related defects at the GaAsSb/GaAs interfaces of the samples considered.

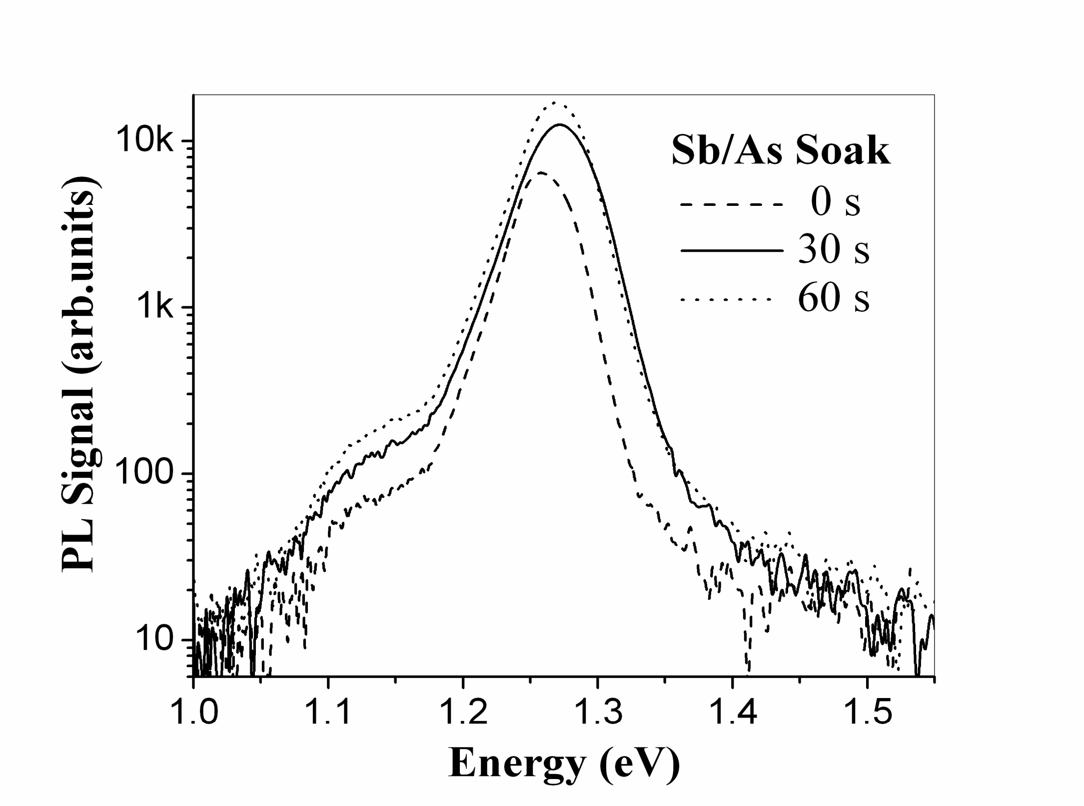

Figure 34. Photoluminescence spectra for the three samples A (0s), B (30s) and C (60s) taken at 80K. The vertical line corresponds to the predicted emission energy for 16% GaAsSb.

Closer inspection of the main peaks also indicates that for each sample there is not a single peak but a superposition of two peaks close in emission energies. This corresponds well with the proposed band diagram presented earlier, which predicts a type II GaAs Conduction Band (CB) to GaAsSb heavy hole

(HH) confined state transition at 1.23 eV and a type I GaAsSb CB to confined HH state transition 57 meV above that. In addition there is a transition between the GaAs Cb and GaAsSb light hole (LH) confined state predicted at 1.32 eV, however, the presence of this transition is not clearly indicated in the PL results. The PL spectra for each sample at 80 K were fitted using Gaussian functions for each of the four peaks just discussed i.e. a low energy peak, the two main peaks and the higher energy LH peak.

A graphical representation of the results for sample A (0 s) is also displayed in Figure 33 with the following labeling now used: peak 1 is the low energy peak associated with Sb related defects, peak 2 is the type II transition between the GaAs CB and GaAsSb HH confined ground state, peak 3 is the type I transition between the GaAsSb Cb and the GaAsSb HH confined ground state. Peak 4 is included to show the location of this transition, but the influence of this peak can be neglected and so the parameters for peak 4 are not included in Table 4. Similar results followed for the other two samples.

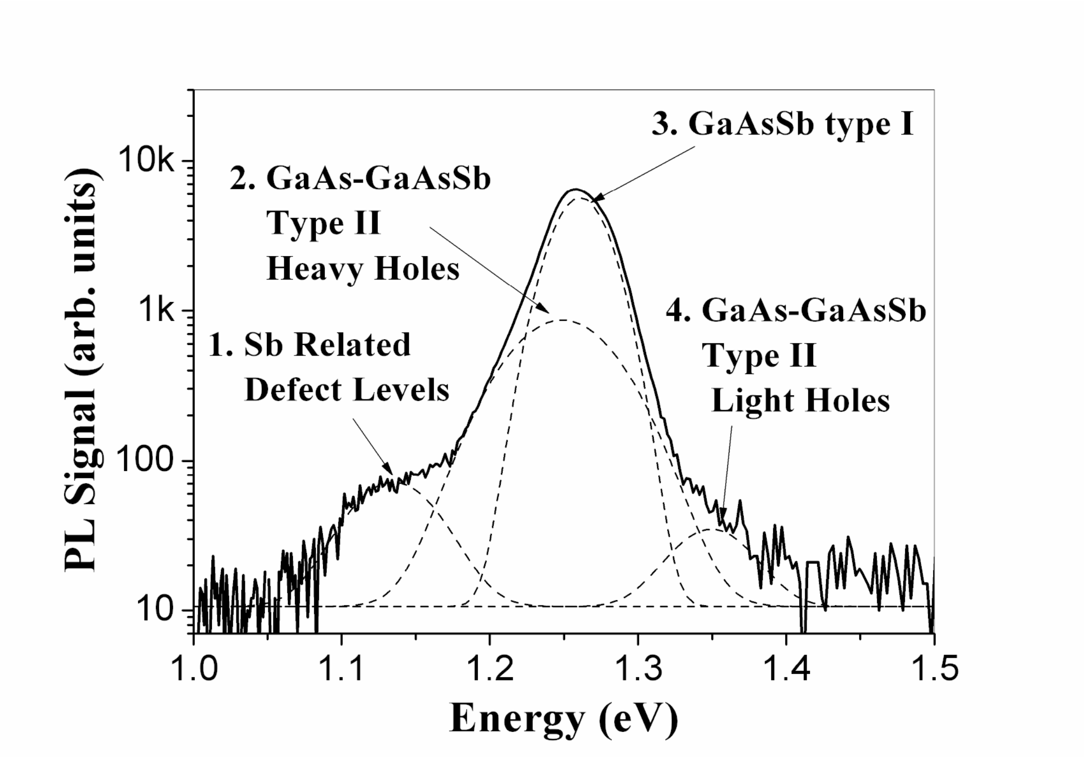

Figure 35. Graphical summary of best fit results for sample A (0 s) using Gaussian functions for the four peaks indicated. Similar results were found for the 30 s and 60 s samples.

There are a number of features of these results that should be commented on. Firstly, peaks 2 and 3 are very close together with a difference in emission energy of at most 12 meV (for sample A) based on the fitting results. This is smaller than the 57 meV predicted by our band calculations, but these calculations do not take into account band bending due to accumulation of carriers at the interfaces, an effect seen in similar studies[88],[89]. The higher FWHM seen for peak 2 as compared to peak 3 in all the samples suggests that the assumption that peak 2 corresponds to a type II transition is valid. The emission energies found for peak 2 in all of the samples agree well with results reported for 5 nm GaAsSb/GaAs quantum wells reported by Peter et al.[90]. Finally, it can be seen that the relative strengths of peaks 2 and 3 changes between samples. Whilst for sample A the ratio of counts for peak 3 to counts for peak 2, hereafter denoted *R*, is roughly 3.4, it drops to 1.6 for B and 1.75 for C.

The relative strengths of the main peaks (peaks 2 and 3) for each of the samples can be understood by considering the effect of the Sb/As soak time on the band structure at the interfaces. In previous investigations it was established that the growth temperature and Sb/As flux ratio will influence the nature of the compositional change in the region of the GaAs-GaAsSb interface[81]. For the case of 0 s soak time, this means the change in composition will not be completely abrupt, but will continue to increase until it reaches a saturation value set by the steady state Sb/As flux ratio. Conversely, for the 60 s soak time, the composition of the GaAsSb will be high at the interface and fall off towards the steady state composition value. The 30 s soak time would be expected to give something closer to the ideal with an abrupt change in composition that is immediately at the steady state composition. The inferred band structures for the 0 s and 60 s samples are shown in Figure 34. As shown, for the 0s case the transition from GaAs to GaAsSb is gradual and the band structure is smoothed to reflect this. The step in the CB is rounded, as are the edges of the Valence Band (VB) confinement well. For the 60 s case a spike is seen in the CB, indicating a higher Sb content at the interface, along with a sharp dip in the VB well. A rounded edge is also included at the GaAs side of the interface to include the effect of the monolayer spikes inferred from the XRD results.

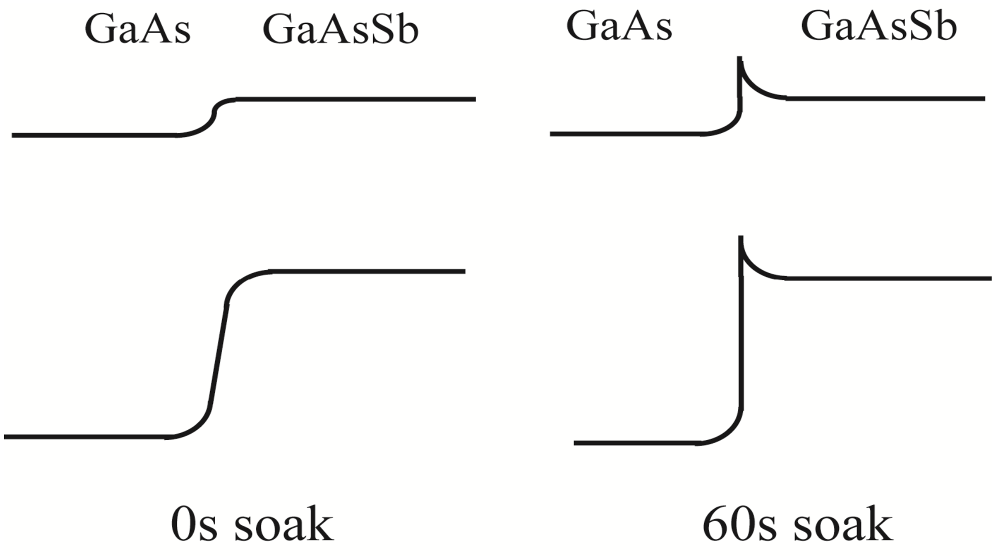

Figure 36. Deduced band structure at the GaAs-GaAsSb interface for 0s and 60s soak times.

The relative emission intensities of the two main peaks in all three samples can be understood by keeping in mind these features of the band structure at the interfaces. For sample A (0 s) the band steps are rounded meaning the carrier densities are expected to be relatively low and it is easier for electrons to escape from the GaAs CB to the GaAsSb CB. The barrier seen for the holes in the GaAsSb confined states is also slightly reduced meaning the confinement of holes is weakest in this sample. For these reasons one can expect the overall intensity for A to be the lowest of the three samples, and why the intensity of peak 3 is much stronger than that of peak 2 i.e. *R* is high. For sample B the carrier densities on both sides of the GaAs-GaAsSb interface will be higher meaning peak 2 increases and since there is no barrier to electrons dropping down to the GaAs CB edge *R* will be the lowest of all the samples. Since the VB confinement potential is sharper than for sample A more holes are expected to be confined and so a greater overall intensity is expected in comparison to sample A but with R being the lowest of all the samples. Finally, for sample C (60 s) the carrier density around the dips in the bands will be higher meaning peak 2 should be stronger since there are a greater number of carriers on both sides of the GaAs-GaAsSb interface. However, the spike in the GaAsSb CB will also mean carriers at this band edge will be more likely to stay there and recombine meaning peak 3 would also increase. This explains why R is significantly reduced in comparison to sample A but remains above that for B. Finally, the strong confinement of the holes due to the sharp dip in the VB edge in the GaAsSb means the hole density would be highest in this sample. From these reasons it follows that sample C has the greatest overall intensity of all the samples.

The conclusion that can be drawn from both the XRD and PL results is that the 30 s soak time gives the sharpest interface between the GaAs and GaAsSb both in terms of interface roughness and compositional abruptness. The XRD results agree with earlier observations of elongated steps at the growth surface when growing GaSb on GaAs [91] or exploiting the exchange reaction between Sb and As[84] but further experimentation to confirm this feature should be undertaken. *In-situ* techniques such as detailed analysis of the RHEED pattern during growth, as well as Transmission Electron Microscopy, may be used to this end.

These results suggest that consideration of the Sb/As soak time must be given when the sharpness of the GaAsSb/GaAs is critical. Whilst the results presented here show that a 30 s soak time seems to give the best result it cannot be ruled out that further optimization is possible. The growth temperature used in this study (500 C) is established as being close to ideal in terms of obtaining a sharp compositional interface but it may be that different growth temperatures are required, which would mean a different optimum soak time. Additionally, it is expected that the relative flux level of the Sb compared to the As would also influence the optimum time since this would influence rate of Sb/As exchange[92]. In summary, the optimum soak time would need to be established for each unique set of growth conditions.

11.4 Conclusion

Multiple quantum well GaAsSb/GaAs heterostructures have been grown with different Sb/As soak times immediately prior to growth of GaAsSb. Using high resolution X-ray diffraction the influence of the soak time on the properties of the GaAsSb/GaAs interface was studied. When X-ray diffraction reciprocal space maps were taken for each sample in the [110] and [1-10] directions, the maps taken in the [1-10] showed the 30 s soak time giving the lowest amount of diffuse scattering around the superlattice peaks. This diffuse scattering was attributed to a corrugated GaAsSb/GaAs interface with the long axis of this corrugation in the [110] direction. The results indicate that a 30 s soak time gives the best result in terms of minimizing this corrugation. Band diagrams for each sample were inferred using these results and the results of a four band k.p model based on the model solid theory. Fitting of Photoluminescence spectra taken at 80 K based on these band diagrams suggests the band structures predicted are valid, though further studies are required. It is concluded that for these growth conditions a 30 s Sb/As soak time immediately prior to growth of GaAsSb on

GaAs is optimal both in terms of interface roughness and compositional abruptness. Because of the temperature dependence of the exchange reaction between Sb and As the optimum soak time would need to be determined for each growth temperature.

Chapter 12

CONCLUSION

The thesis discussed solar cells based on heterostructure in detail. A novel theory describing the operation of silicon based heterostructure with particular emphasis on a-Si/c-Si heterojunction is outlined. The main premise of the theory is that an inversion region is present at the interface between a-Si and c-Si and the presence of inversion region affects the device performance. Theoretical modeling a portion of which included the use of commercial simulator Sentaurus was performed to study the effect of inversion region in device characteristics. Experimental results were provided to corroborate the findings of theoretical modeling. A novel device concept that can realize the theoretical maximum efficiency of silicon solar cells was also proposed. The thesis outlined a characterization scheme for optimization of the hetero-interface in silicon based heterostructure through lifetime spectroscopy. The work on nanostructured medium involves identifying the material combinations for a MQFL system involving quantum well. The combination of AlinAs as the barrier and InAsP as well was found to be the ideal material combination. The absorption coefficient calculations performed on the material combination show that the absorption coefficients determining the rates of transition in the quantum well balance each other, thereby increasing the possibility of attaining a MQFL system. The growth of GaAsSb by molecular beam epitaxy was describwed in detail. Also, the optimization of GaAsSb and GaAs interface was experimentally studied and it was found out that a growth interruption of 30 seconds between the growth of GaAsSb and GaAs gives the sharpest interface.

REFERENCES

[1] Zhao, Jianhua, Aihua Wang, and Martin A Green. "24·5% Efficiency silicon PERT cells on MCZ substrates and 24·7% efficiency PERL cells on FZ substrates." *Progress in Photovoltaics: Research and Applications* 7, no. 6 (November 1, 1999): 471-474

[2] Swanson, R. M. "Approaching the 29% limit efficiency of silicon solar cells." In *Conference Record of the Thirty-first IEEE Photovoltaic Specialists Conference, 2005*, 889- 894. IEEE, 2005.

[3] European Photovoltaic Industry Association. (2010). *EPIA Roadmap*. Retrieved from http://www2.epia.org/documents/Roadmap_EPIA.pdf.

[4] Tanaka, M., S. Okamoto, S. Tsuge, and S. Kiyama. "Development of hit solar cells with more than 21% conversion efficiency and commercialization of highest performance hit modules." In *Proceedings of 3rd World Conference on Photovoltaic Energy Conversion, 2003*, 1:955-958 Vol.1. IEEE, 2003.

[5] Tanaka, Makoto, Mikio Taguchi, Takao Matsuyama, Toru Sawada, Shinya Tsuda, Shoichi Nakano, Hiroshi Hanafusa, and Yukinori Kuwano. "Development of New a-Si/c-Si Heterojunction Solar Cells: ACJ-HIT (Artificially Constructed Junction-Heterojunction with Intrinsic Thin-Layer)." *Japanese Journal of Applied Physics* 31, no. Part 1, No. 11 (November 1992): 3518-3522.

[6] Lu, M, Ph.D. Thesis, University of Delaware, 2008

[7] Luque, Antonio, and Antonio Martí. "Increasing the Efficiency of Ideal Solar Cells by Photon Induced Transitions at Intermediate Levels." *Physical Review Letters* 78, no. 26 (June 30, 1997): 5014.

[8] Stangl, R., A. Froitzheim, M. Schmidt, W. Fuhs. "Design Criteria For Amorphous/Crystalline Silicon Heterojunction Solar Cells - A Simulation Study." *3rd World Conference on Photovoltaic Energy Conversion*, May 11-18, 2003 Osaka, Japan.

[9] Centurioni, E., and D. Iencinella. "Role of front contact work function on amorphous silicon/crystalline silicon heterojunction solar cell performance." *IEEE Electron Device Letters* 24, no. 3 (March 2003): 177- 179.

[10] Matsuura, Hideharu, Tetsuhiro Okuno, Hideyo Okushi, and Kazunobu Tanaka. "Electrical properties of n-amorphous/p-crystalline silicon heterojunctions." *Journal of Applied Physics* 55, no. 4 (1984): 1012.

[11] Slade, A. “Boron Tribromide Sourced Boron Diffusions for Silicon Solar Cells”, PhD thesis.

[12] Yablonovitch, E., D. L. Allara, C. C. Chang, T. Gmitter, and T. B. Bright. “Unusually Low Surface-Recombination Velocity on Silicon and Germanium Surfaces.” *Physical Review Letters* 57, no. 2 (July 14, 1986): 249.

[13] Häcker, Rolf, and Andreas Hangleiter. “Intrinsic upper limits of the carrier lifetime in silicon.” *Journal of Applied Physics* 75, no. 11 (1994): 7570.

[14] Huldt, L., N. G. Nilsson, and K. G. Svantesson. “The temperature dependence of band-to-band Auger recombination in silicon.” *Applied Physics Letters* 35, no. 10 (1979): 776.

[15] Schropp, Ruud E. I., and Miro Zeman. *Amorphous and microcrystalline silicon solar cells: modeling, materials, and device technology*. Springer, 1998.

[16] Muller, Richard S., Theodore I. Kamins, and Mansun Chan. *Device electronics for integrated circuits*. John Wiley & Sons, 2003.

[17] Sebastiani, M., L. Di Gaspare, G. Capellini, C. Bittencourt, and F. Evangelisti. “Low-Energy Yield Spectroscopy as a Novel Technique for Determining Band Offsets: Application to the c-Si(100)/a-Si:H Heterostructure.” *Physical Review Letters* 75, no. 18 (October 30, 1995): 3352.

[18] Fritzsche, H., and K. -J. Chen. “Drift-mobility measurements in amorphous semiconductors using traveling-wave method.” *Physical Review B* 28, no. 8 (October 15, 1983): 4900.

[19] Tiedje, T., J. M. Cebulka, D. L. Morel, and B. Abeles. “Evidence for Exponential Band Tails in Amorphous Silicon Hydride.” *Physical Review Letters* 46, no. 21 (May 25, 1981): 1425..

[20] Powell, M. J., and S. C. Deane. “Improved defect-pool model for charged defects in amorphous silicon.” *Physical Review B* 48, no. 15 (October 15, 1993): 10815.

[21] Meaudre, M, and R Meaudre. “Determination of the capture cross sections of electrons in undoped hydrogenated amorphous silicon from the photoconductivity of and space-charge relaxation in n^+-i-n^+ structures; the role of light exposure and annealing.” *Journal of Physics: Condensed Matter* 13, no. 24 (June 2001): 5663-5673.

[22]Kim, J.C. and R.J. Schwartz, "Parameter estimation and modeling of hydrogenated amorphous silicon", *Electrical and Computer Engineering, ECE Technical Reports, Purdue Libaries*,1996.

[23]Abeles, B., C. R. Wronski, Y. Goldstein, and G. D. Cody. "Capture cross-section and density of deep gap states in a-SiHx schottky barrier structures." *Solid State Communications* 41, no. 3 (January 1982): 251-253.

[24]Hartke, J. L. "The Three-Dimensional Poole-Frenkel Effect." *Journal of Applied Physics* 39, no. 10 (1968): 4871.

[25]Vaillant, F., and D. Jousse. "Recombination at dangling bonds and steady-state photoconductivity in a-Si:H." *Physical Review B* 34, no. 6 (1986): 4088.

[26]Schiff, E.A. "Hole mobilities and the physics of amorphous silicon solar cells." *Journal of Non-Crystalline Solids* 352, no. 9-20 (June 15, 2006): 1087-1092.

[27]Green, M.A., F.D. King, and J. Shewchun. "Minority carrier MIS tunnel diodes and their application to electron- and photo-voltaic energy conversion--I. Theory." *Solid-State Electronics* 17, no. 6 (June 1974): 551-561.

[28]Olibet, Sara, Evelyne Vallat-Sauvain, and Christophe Ballif. "Model for a-Si:H/c-Si interface recombination based on the amphoteric nature of silicon dangling bonds." *Physical Review B* 76, no. 3 (July 23, 2007): 035326.

[29]Schroder, Dieter K. *Semiconductor material and device characterization*. John Wiley and Sons, 2006.

[30]Tanaka, Makoto, Mikio Taguchi, Takao Matsuyama, Toru Sawada, Shinya Tsuda, Shoichi Nakano, Hiroshi Hanafusa, and Yukinori Kuwano. "Development of New a-Si/c-Si Heterojunction Solar Cells: ACJ-HIT (Artificially Constructed Junction-Heterojunction with Intrinsic Thin-Layer)." *Japanese Journal of Applied Physics* 31, no. Part 1, No. 11 (November 1992): 3518-3522.

[31]Tanaka, M., S. Okamoto, S. Tsuge, and S. Kiyama. "Development of hit solar cells with more than 21% conversion efficiency and commercialization of highest performance hit modules." In *Proceedings of 3rd World Conference on Photovoltaic Energy Conversion, 2003*, 1:955-958 Vol.1. IEEE, 2003.

[32] "Sinton Lifetime tester Manual"

[33]Street, R. A. *Hydrogenated amorphous silicon*. Cambridge University Press, 1991.

[34] Winer, K., I. Hirabayashi, and L. Ley. “Exponential Conduction-Band Tail in P-Doped a-Si:H.” *Physical Review Letters* 60, no. 25 (June 20, 1988): 2697.

[35] Y. L. Main, J. M. Marshall, and S. Reynolds, “Computer modeling of multi-trapping and hopping transport in disordered semiconductors,” *Journal of Optoelectronics and Advanced Materials* 7, no. 1 (2005): 107

[36] Marshall J. M. “Charge carrier thermalization by hopping in band tails at zero temperature.” *Philosophical Magazine Letters* 80, no. 12 (2000): 777-784.

[37] Vasileska, Dragica, and Stephen Marshall Goodnick. *Computational electronics*. Morgan & Claypool Publishers, 2006.

[38] Jegert, Gunther, Alfred Kersch, Wenke Weinreich, Uwe Schröder, and Paolo Lugli. “Modeling of leakage currents in high-κ dielectrics: Three-dimensional approach via kinetic Monte Carlo.” *Applied Physics Letters* 96, no. 6 (2010): 062113.

[39] Littlejohn, M. A. “Electron transport in planar-doped barrier structures using an ensemble Monte Carlo method.” *Journal of Vacuum Science & Technology B: Microelectronics and Nanometer Structures* 1, no. 2 (1983): 449.

[40] Jacoboni, Carlo, and Paolo Lugli. *The Monte Carlo method for semiconductor device simulation*. Springer, 1989.

[41] Larcher, L. “Statistical simulation of leakage currents in MOS and flash memory devices with a new multiphonon trap-assisted tunneling model.” *IEEE Transactions on Electron Devices* 50, no. 5 (May 2003): 1246- 1253.

[42] Blank, O., H. Reisinger, R. Stengl, M. Gutsche, F. Wiest, V. Capodieci, J. Schulze, and I. Eisele. “A model for multistep trap-assisted tunneling in thin high-k dielectrics.” *Journal of Applied Physics* 97, no. 4 (2005): 044107.

[43] Suzuki, Eiichi, Dieter K. Schroder, and Yutaka Hayashi. “Carrier conduction in ultrathin nitrided oxide films.” *Journal of Applied Physics* 60, no. 10 (1986): 3616.

[44] Kleider, J. P., A. S. Gudovskikh, and P. Roca i Cabarrocas. “Determination of the conduction band offset between hydrogenated amorphous silicon and crystalline silicon from surface inversion layer conductance measurements.” *Applied Physics Letters* 92, no. 16 (2008): 162101.

[45] Sze, S. M., and Kwok Kwok Ng. *Physics of semiconductor devices*. John Wiley and Sons, 2007.

[46] Taguchi, Mikio, Eiji Maruyama, and Makoto Tanaka. “Temperature Dependence of Amorphous/Crystalline Silicon Heterojunction Solar Cells.” *Japanese Journal of Applied Physics* 47, no. 2 (February 2008): 814-818.

[47] Froitzheim, A, K Brendel, L Elstner, W Fuhs, K Kliefoth, and M Schmidt. “Interface recombination in heterojunctions of amorphous and crystalline silicon.” *Journal of Non-Crystalline Solids* 299-302, no. Part 1 (April 2002): 663-667.

[48] Sakata, Isao, and Hitoshi Kawanami. “Band Discontinuities in Gallium Phosphide/Crystalline Silicon Heterojunctions Studied by Internal Photoemission.” *Applied Physics Express* 1 (August 2008): 091201.

[49] Buriak, Jillian M. “Organometallic Chemistry on Silicon and Germanium Surfaces.” *Chemical Reviews* 102, no. 5 (May 1, 2002): 1271-1308.

[50] Bent, Stacey F. “Organic functionalization of group IV semiconductor surfaces: principles, examples, applications, and prospects.” *Surface Science* 500, no. 1-3 (March 10, 2002): 879-903.

[51] Hamers, Robert J., Sarah K. Coulter, Mark D. Ellison, Jennifer S. Hovis, David F. Padowitz, Michael P. Schwartz, C. Michael Greenlief, and John N. Russell. “Cycloaddition Chemistry of Organic Molecules with Semiconductor Surfaces.” *Accounts of Chemical Research* 33, no. 9 (2000): 617-624.

[52] Taguchi, Mikio, Akira Terakawa, Eiji Maruyama, and Makoto Tanaka. “Obtaining a higher Voc in HIT cells.” *Progress in Photovoltaics: Research and Applications* 13, no. 6 (September 1, 2005): 481-488.

[53] Green, M. A. “Limits on the open-circuit voltage and efficiency of silicon solar cells imposed by intrinsic Auger processes.” *IEEE Transactions on Electron Devices* 31, no. 5 (May 1984): 671- 678.

[54] Ghosh, Kunal, Clarence J. Tracy, Stanislau Herasimenka, Christiana Honsberg, and Stuart Bowden. “Explanation of the device operation principle of amorphous silicon/ crystalline silicon heterojunction solar cell and role of the inversion of crystalline silicon surface.” In *2010 35th IEEE Photovoltaic Specialists Conference*, 001383-001386. Honolulu, HI, USA, 2010.

[55] Cleef, Maarten W. M. van, Francisco A. Rubinelli, Rita Rizzoli, Roberto Pinghini, Ruud E. I. Schropp, and Werner F. van der Weg. “Amorphous Silicon Carbide/Crystalline Silicon Heterojunction Solar Cells: A Comprehensive Study of the Photocarrier Collection.” *Japanese Journal of Applied Physics* 37, no. Part 1, No. 7A (July 1998): 3926-3932.

[56] Girisch, R. B.M, R. P Mertens, and R. F De Keersmaecker. "Determination of Si-SiO2 interface recombination parameters using a gate-controlled point-junction diode under illumination." *IEEE Transactions on Electron Devices* 35, no. 2 (February 1988): 203-222.

[57] S. K. Pang and A. Rohatgi, "A new methodology for separating Shockley–Read–Hall lifetime and Auger recombination coefficients from the photoconductivity decay technique," *Journal of Applied Physics*, vol. 74, p. 5554, 1993.

[58] D. K. Schroder, "Carrier lifetimes in silicon," *IEEE Transactions on Electron Devices*, vol. 44, no. 1, pp. 160-170, Jan. 1997.

[59] Landsberg, Peter T. *Recombination in Semiconductors*. Cambridge University Press, 2003.

[60] Trupke, T., M. A. Green, P. Würfel, P. P. Altermatt, A. Wang, J. Zhao, and R. Corkish. "Temperature dependence of the radiative recombination coefficient of intrinsic crystalline silicon." *Journal of Applied Physics* 94, no. 8 (2003): 4930.

[61] Marti, A., L. Cuadra, and A. Luque. "Quantum dot intermediate band solar cell." In *Conference Record of the Twenty-Eighth IEEE Photovoltaic Specialists Conference, 2000*, 940-943. IEEE, 2000.

[62] Levy, M. Y, and C. Honsberg. "Nanostructured Absorbers for Multiple Transition Solar Cells." *IEEE Transactions on Electron Devices* 55, no. 3 (March 2008): 706-711.

[63] Dahal, Som N, Stephen P Bremner, and Christiana B Honsberg. "Identification of candidate material systems for quantum dot solar cells including the effect of strain." *Progress in Photovoltaics: Research and Applications* 18, no. 4 (June 1, 2010): 233-239.

[64] Nelson, Jenny. *The physics of solar cells*. Imperial College Press, 2003.

[65] Levine, B. F. "Quantum-well infrared photodetectors." *Journal of Applied Physics* 74, no. 8 (1993): R1.

[66] Serdiukova, I., C. Monier, M. F. Vilela, and A. Freundlich. "Critical built-in electric field for an optimum carrier collection in multiquantum well p-i-n diodes." *Applied Physics Letters* 74, no. 19 (1999): 2812.

[67]Bremner, Stephen P., Michael Y. Levy, and Christiana B. Honsberg. “Limiting efficiency of an intermediate band solar cell under a terrestrial spectrum.” *Applied Physics Letters* 92, no. 17 (2008): 171110.

[68]Vurgaftman, I., J. R. Meyer, and L. R. Ram-Mohan. “Band parameters for III–V compound semiconductors and their alloys.” *Journal of Applied Physics* 89, no. 11 (2001): 5815.

[69]Fong, C. Y., W. Weber, and J. C. Phillips. “Violation of Vegard’s law in covalent semiconductor alloys.” *Physical Review B* 14, no. 12 (December 15, 1976): 5387.

[70]Adachi, Sadao. “GaAs, AlAs, and AlxGa1-xAs Material parameters for use in research and device applications.” *Journal of Applied Physics* 58, no. 3 (August 1985): R1-R29.

[71]Bir, Gennadiĭ Levikovich, and Grigoriĭ Ezekielevich Pikus. *Symmetry and strain-induced effects in semiconductors*. Wiley, 1974.

[72]Vos, Alexis de. *Endoreversible thermodynamics of solar energy conversion*. Oxford University Press, 1992.

[73]Levy, Michael Y., and Christiana Honsberg. “Rapid and precise calculations of energy and particle flux for detailed-balance photovoltaic applications.” *Solid-State Electronics* 50, no. 7-8 (July): 1400-1405.

[74]Bremner, S. P, R. Corkish, and C. B Honsberg. “Detailed balance efficiency limits with quasi-Fermi level variations [QW solar cell].” *IEEE Transactions on Electron Devices* 46, no. 10 (October 1999): 1932-1939.

[75]Shockley, William, and Hans J. Queisser. “Detailed Balance Limit of Efficiency of p-n Junction Solar Cells.” *Journal of Applied Physics* 32, no. 3 (1961): 510.

[76]Choi, K. K. *The physics of quantum well infrared photodetectors*. World Scientific, 1997.

[77]Levy, Michael Y, and Christiana Honsberg. “Absorption coefficients of intermediate-band media.” *Journal of Applied Physics* 106, no. 7 (October 2009): 073103-073103-12.

[78]Fox, Anthony Mark. *Optical properties of solids*. Oxford University Press, 2010.

[79]Wood, D. M., and Alex Zunger. “Composition pinning in epitaxial alloys.” *Physical Review B* 38, no. 17 (December 15, 1988): 12756.

[80]André, R., S. Wey, and C. W. Tu. “Competition between As and P for incorporation during gas-source molecular beam epitaxy of InGaAsP.” *Journal of Crystal Growth* 235, no. 1-4 (February 2002): 65-72.

[81]Kaspi, Ron, and Keith R. Evans. “Sb-surface segregation and the control of compositional abruptness at the interface.” *Journal of Crystal Growth* 175-176, no. Part 2 (May 1, 1997): 838-843.

[82]Hall, E. “Operational experience with a valved antimony cracker source for use in molecular beam epitaxy.” *Journal of Vacuum Science & Technology B: Microelectronics and Nanometer Structures* 16 (September 1998): 2660.

[83]Gailhanou, M., T. Baumbach, U. Marti, P. C. Silva, F. K. Reinhart, and M. Ilegems. “X-ray diffraction reciprocal space mapping of a GaAs surface grating.” *Applied Physics Letters* 62 (1993): 1623.

[84]Kanto, Toru, and Koichi Yamaguchi. “In-plane self-arrangement of high-density InAs quantum dots on GaAsSb/GaAs(001) by molecular beam epitaxy.” *Journal of Applied Physics* 101 (2007): 094901.

[85]Van de Walle, Chris G. “Band lineups and deformation potentials in the model-solid theory.” *Physical Review B* 39, no. 3 (January 15, 1989): 1871.

[86]Cusack, M. A., P. R. Briddon, and M. Jaros. “Electronic structure of InAs/GaAs self-assembled quantum dots.” *Physical Review B* 54, no. 4 (July 15, 1996): R2300.

[87] Hsu, H P, P Sitarek, Y S Huang, P W Liu, J M Lin, H H Lin, and K K Tiong. “Modulation spectroscopy study of the effects of growth interruptions on the interfaces of GaAsSb/GaAs multiple quantum wells.” *Journal of Physics: Condensed Matter* 18 (July 5, 2006): 5927-5935.

[88] Luo, X. D., C. Y. Hu, Z. Y. Xu, H. L. Luo, Y. Q. Wang, J. N. Wang, and W. K. Ge. “Selectively excited photoluminescence of GaAs[sub 1−x]Sb[sub x]/GaAs single quantum wells.” *Applied Physics Letters* 81 (2002): 3795.

[89]Teissier, R., D. Sicault, J. C. Harmand, G. Ungaro, G. Le Roux, and L. Largeau. “Temperature-dependent valence band offset and band-gap energies of pseudomorphic GaAsSb on GaAs.” *Journal of Applied Physics* 89 (2001): 5473.

[90]Peter, M., K. Winkler, M. Maier, N. Herres, J. Wagner, D. Fekete, K. H. Bachem, and D. Richards. “Realization and modeling of a pseudomorphic (GaAs1−xSbx–InyGa1−yAs)/GaAs bilayer-quantum well.” *Applied Physics Letters* 67 (1995): 2639.

[91] Bennett, B.R., B.V. Shanabrook, P.M. Thibado, L.J. Whitman, and R. Magno. "Stranski-Krastanov growth of InSb, GaSb, and AlSb on GaAs: structure of the wetting layers." *Journal of Crystal Growth* 175-176, no. 2 (May 1, 1997): 888-893.

[92] Miura, Takeshi, Takanori Nakai, and Koichi Yamaguchi. "Atomically-controlled GaSb-termination of GaAs surface and its properties." *Applied Surface Science* 237, no. 1-4 (October 15, 2004): 242-245.